

Received 19 August 2025, accepted 22 September 2025, date of publication 3 October 2025, date of current version 16 October 2025.

Digital Object Identifier 10.1109/ACCESS.2025.3617230



## RESEARCH ARTICLE

# A New Image Sharpening Filter Based on Gradient and Retinex-Inspired Contrast

MICHELA LECCA<sup>ID</sup><sup>1</sup>, MASSIMO GOTTARDI<sup>ID</sup><sup>2</sup>, (Member, IEEE), AND PAOLA LECCA<sup>ID</sup><sup>3,4</sup>

<sup>1</sup>Center for Digital Industry, Technologies of Vision, Fondazione Bruno Kessler, 38123 Trento, Italy

<sup>2</sup>Center for Sensors and Devices, Integrated Readout ASICs and Image Sensors, Fondazione Bruno Kessler, 38123 Trento, Italy

<sup>3</sup>Faculty of Engineering, Free University of Bozen-Bolzano, 39100 Bolzano, Italy

<sup>4</sup>National Group for Mathematical Analysis, Probability and Their Applications, National Institute of High Mathematics Francesco Severi, 00185 Rome, Italy

Corresponding author: Paola Lecca (Paola.Lecca@unibz.it)

**ABSTRACT** Image edges are essential for understanding and processing the content of the acquired scene, but a clear edge detection is not always possible. Unfavorable environmental conditions, poor lighting, incorrect camera settings and/or vibrations may produce blurry or dark images with unclear content and details. Local spatial filters are integrated into many hardware and software as sharpening tools, but choosing the most adequate filter and its parameters is usually non trivial. This work proposes a new filter, whose kernel is computed by comparing over a pre-defined window the image Prewitt gradient with an image contrast measure inspired by Retinex theory. The experiments, carried out on public real-world images with different edge visibility, show that the proposed image-aware filter efficaciously increases the edge visibility with low computational cost and performs better than a standard Laplacian filter. As an usage example, the sharpening filter is here applied to medical images of retinal fundus: improving the clarity and detail of these images is essential for visualizing and analysing anatomical structures, identifying abnormalities, and assisting in diagnosis and treatments. Finally, a hardware architecture of the sharpening filter, partially integrating on-chip the gradient and contrast computation, is outlined. Such an integration could be beneficial for enhancing in real-time the quality of pictures captured by devices with limited power resources, with an average consumption of  $\sim 28 \mu\text{W}$  and  $\sim 30 \text{ kb}$  of embedded memory in case of a color VGA image. The data obtained in filter validation experiments show a marked increase in the Prewitt's gradient magnitudes in 100% of cases and in the edge thickness in a percentage ranging from 73.3% to 100% of cases, without visibly affecting the image naturalness.

**INDEX TERMS** Edge detection, image contrast, image sharpening, local spatial filters.

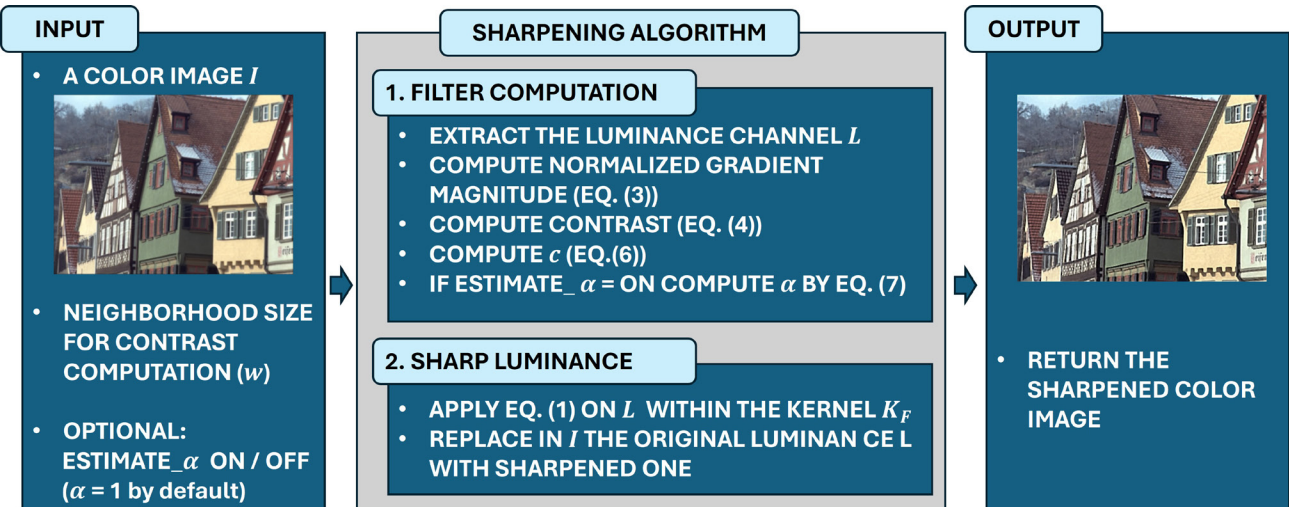
## I. INTRODUCTION

Image edges are local variations of image intensity. Their detection is of primary importance to allow humans and vision systems to understand content and details of the acquired scene. In fact, edges may represent object boundaries, texture elements, changes in spatial depth or in light. Edges are exploited by many algorithms, e.g., for recognizing objects and people [1], [2], [3], interpreting medical images [4], [5], and improving the quality of images captured under bad light conditions [6], [7], [8]. An accurate

The associate editor coordinating the review of this manuscript and approving it for publication was Chao Zuo<sup>ID</sup>.

edge detection is thus highly desired, however this task may be hampered by several factors, like e.g. environmental conditions, bad illumination, camera wrong settings and/or vibrations, which produce blurred images, with weak edges and poorly readable content and details.

Image sharpening is the image processing branch devoted to enhanced the image local contrast and texture, making edges more visible. Image sharpening can be achieved in different ways, for instance by improving the overall image quality [9], [10], [11], by re-working the image in the frequency domain [12], [13], or by applying local spatial filters, like Laplacian operator and unsharp masking [14], [15], [16], also combined with the analysis in frequency



**FIGURE 1.** Work-flow of the proposed sharpening approach. The computation of  $c$  is pictorially summarized in Figure 2.

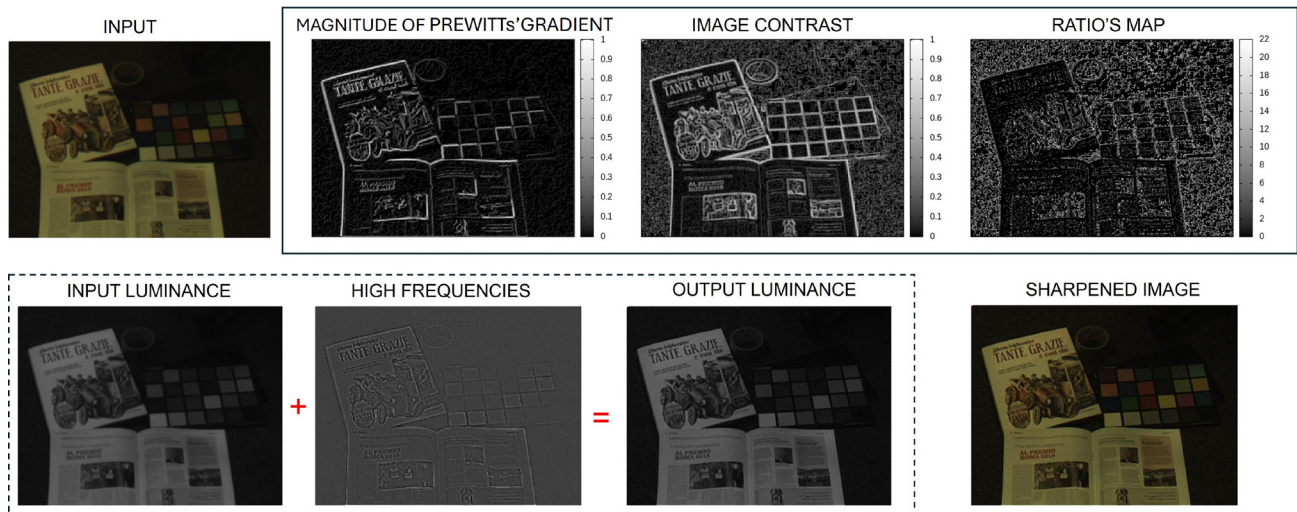


**FIGURE 2.** Main steps of the sharpening algorithm within the proposed estimate of  $c$ : on top, left, the color input image; on top, right, the normalized magnitude of Prewitt's gradient, the Retinex inspired contrast measure  $\varphi$  and the map with  $\rho$  computed pixel by pixel; on bottom, left, the dotted box shows pictorially the terms of Eq. (1), i.e., the luminance  $L$  of the input image, its filtered version and the sharpened luminance  $S$ ; on bottom, right, the color image with sharpened luminance. In this example,  $\alpha = 1$  and  $w = 3$ .

domain [17]. Local spatial filters are included as in-built modules in many cameras and displays and as sharpening tools in many photo- and video-editors, e.g. [18] and [19], because they enable a fast edge enhancement at a low computational cost [16]. The image sharpening based on such filters works as follows. First, the input image (or its luminance)  $L$  is convolved with a high-pass filter, designed to increase the local spatial changes of  $L$  while leaving unchanged uniform regions. Then, the filtered image, usually re-scaled by a positive, real-valued factor, is summed up to  $L$ : the result is a new image with more visible edges. In software tools, the choice of the filter, of its parameters as well as of the scaling factor, which is essential in controlling the sharpening strength, is usually left to the user. Some methods propose to estimate the scaling factor adaptively from image luminance, gradient and blurriness (see e.g. [16], [20]), but they require

making specific assumptions on the blur nature and diffusion, that, in turn, introduce other variables to be carefully tuned. This represents a critical point, since a non-expert user must generally proceed by trial and errors.

This problem is addressed here by introducing a new, discrete, spatial filter, exploiting a single parameter  $c$  estimated without supervision from gradient and contrast information extracted from  $L$ . Since when  $c = 8$  this filter coincides with a numerical approximation of the Laplacian operator, the proposed approach is here referred as to a *Laplacian-like* sharpening. This Laplacian-like approach computes a Retinex-inspired contrast of  $L$  derived from [21] and compares it with the magnitude of the Prewitt gradient of  $L$ . Since this Retinex-inspired contrast enables detecting blurry, slight and low-lighted edges much better than a standard gradient, the pixels whose the contrast exceeds

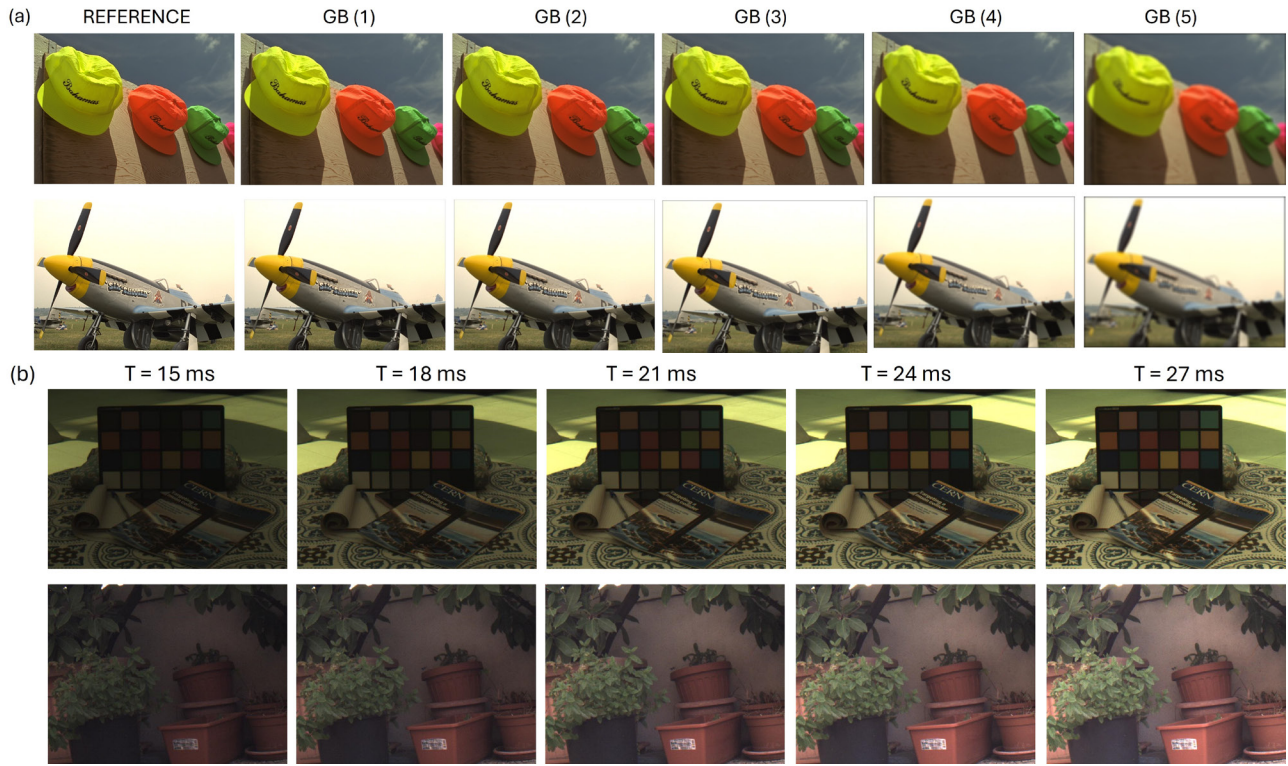


**FIGURE 3.** In (a) two reference images from TID-2013 and their distortions by Gaussian blur (GB) at the levels indicated in the brackets. In (b) two images from MEXICO-2020, each of them captured at five different exposure times (from  $T = 15$  ms to  $T = 27$  ms).

the magnitude of the Prewitt gradient are considered as edges with *improvable visibility* and are used to compute the coefficients of the filter kernel. Precisely, these latter are set as a function of the ratios between the contrast and the Prewitt gradient magnitude of the *improvable* pixels. The use of such features' combination for defining a sharpening filter represents one novelty of the proposed approach. Moreover, the scaling factor used for blending the input image and its filtered version is set to one by default, but another value, estimated without supervision from the image gradient, is also considered. The experiments, conducted on a public dataset of real-world images acquired under different exposure times and with different blur levels, show that the proposed *image-aware* sharpening filter well enhances the image edges, surpassing the results of the Laplacian sharpening, that - due to its mathematical similarity the proposed approach - represents its main competitor but has the disadvantage of leaving the choice of the scale factor to the user. As an usage example, the proposed filter is applied here to medical image of retinal fundus: improving the details of such images is very important to clearly detect the retinal anatomic structures, in particular the blood vessels, and thus assist medical doctors in diagnosis and treatments of possible diseases. Some tests on edge enhancement of remote sensing and compressed images are also provided. Lastly, some considerations on a possible sensor architecture are reported, aimed at integrating the filter on the same silicon die as the

sensor. This approach might enable low-power application scenarios such as Uncrewed Aerial Vehicles (UAV), where the captured images may be blurred due to device instability, weather conditions or atmospheric pollution.

## II. THE PROPOSED IMAGE SHARPENING FILTER

Image sharpening by spatial filters has the following mathematical expression:

$$S(x) = L(x) + \alpha(L * F)(x) \quad (1)$$

where  $L$  is the input image,  $F$  is a high-pass filter,  $\alpha$  is a re-scaling factor strictly greater than zero,  $x$  is an image pixel,  $*$  indicates the convolution operator and  $S$  is the sharpened image.

In this work, image sharpening is reached by setting  $\alpha = 1$  and convolving the image  $L$  (or the luminance channel  $L$  of any color image  $I$ ) with a spatial filter having the following  $3 \times 3$  kernel:

$$K_F = \begin{bmatrix} -\frac{c}{8} & -\frac{c}{8} & -\frac{c}{8} \\ -\frac{c}{8} & c & -\frac{c}{8} \\ -\frac{c}{8} & -\frac{c}{8} & -\frac{c}{8} \end{bmatrix} \quad (2)$$

where  $c$  is a real-valued parameter greater than 1. It is easy to check that this filter amplifies any local variation of  $L$ , while maintains stable the values of  $L$  over uniform regions. Tuning  $c$  enables controlling the sharpening effect: the higher  $c$ , the stronger the sharpening is. Since for  $c = 8$  Equation (1)

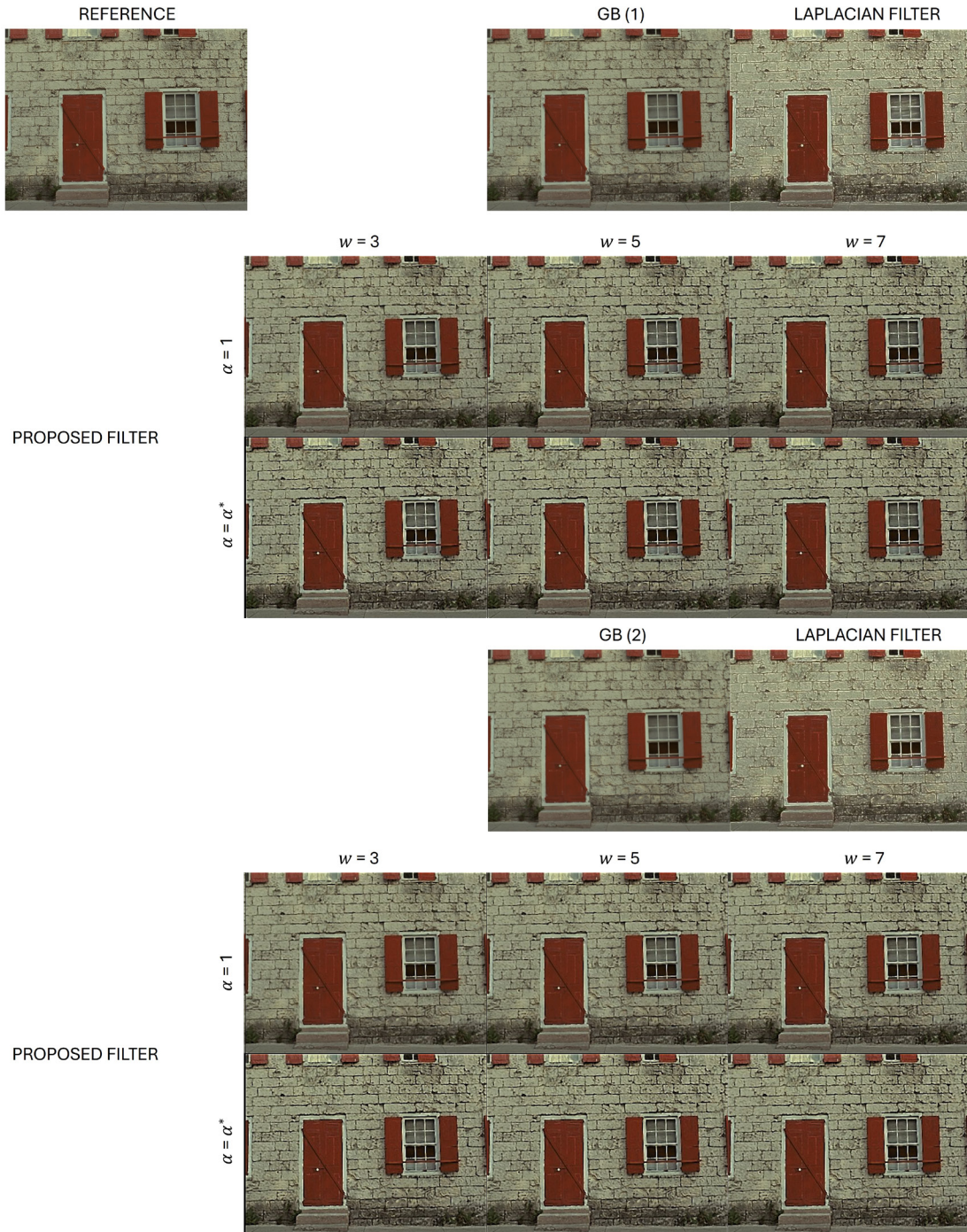


**FIGURE 4.** Laplacian and proposed sharpening applied to an image from TID-2013 (REFERENCE) distorted by Gaussian blur at two different levels GB(1) and GB(2): the Gaussian blur is here very slight, however the proposed approach returns an image whose edges are even more visible than those of the image REFERENCE.

implements the Laplacian sharpening, the proposed filter can be considered as a Laplacian-like operator with the difference that here the coefficient  $c$  is not fixed a-priori, but estimated based on the image gradient and contrast (see Appendix A for mathematical details about the proposed kernel and the Laplacian operator). The work-flow of the proposed sharpening algorithm is depicted in Figure 1, while

the computation of  $c$  is sketched in in Figure 2. Specifically,  $c$  is computed by the following steps:

- 1) *Computation of Prewitt's Gradient Magnitude:* Prewitt's gradient approximates the gradient of  $L$  as

$$\nabla_P L(x) = (L * K_x, L * K_y) \quad (3)$$

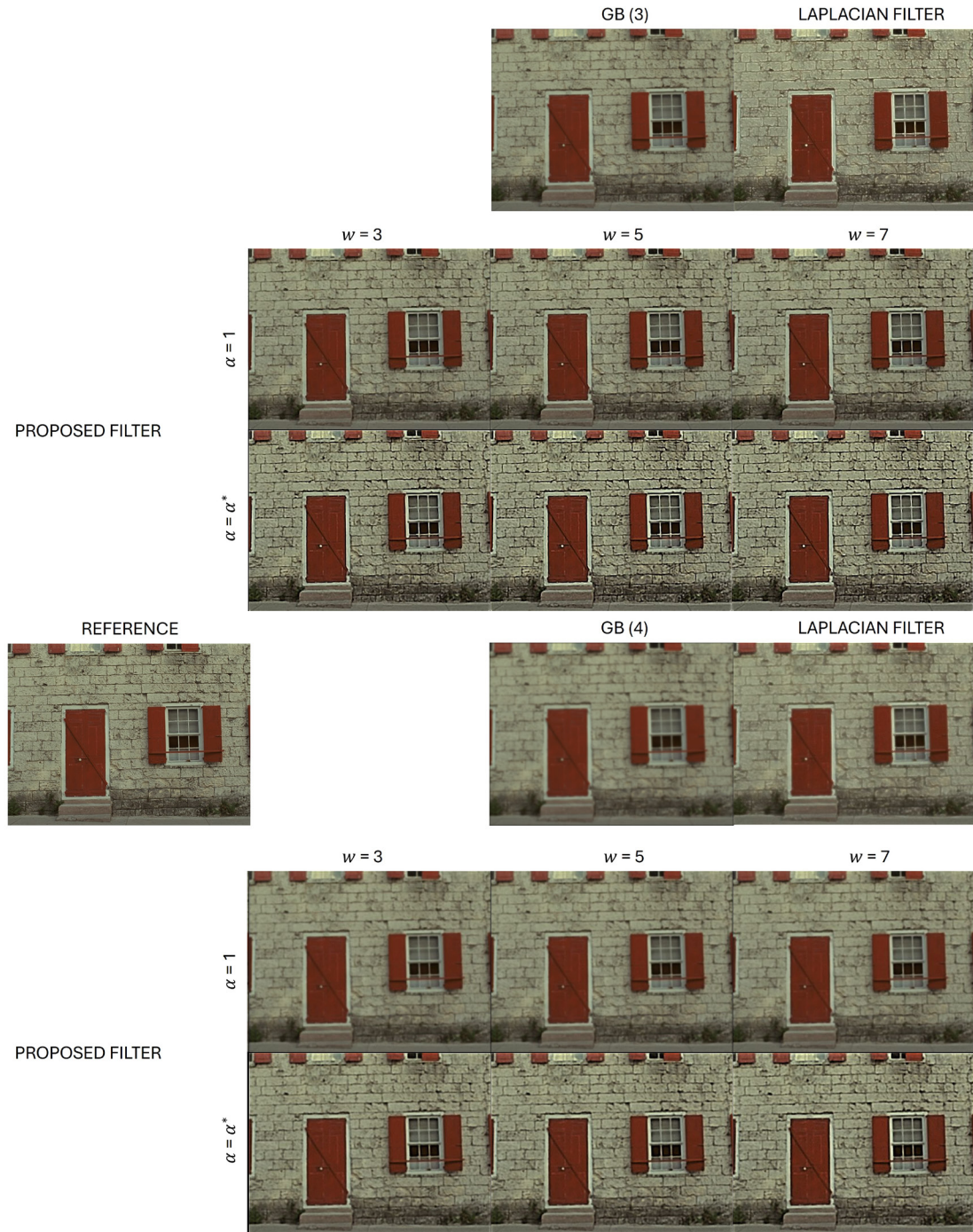


**FIGURE 5.** Laplacian and proposed sharpening applied to an image from TID-2013 (REFERENCE) distorted by Gaussian blur at two different levels GB(3) and GB(4): the edges, that are poorly visible in the distorted images, are well enhanced by the proposed filter, especially for  $\alpha = \alpha^*$ .

where

$$K_x = \begin{bmatrix} -1 & -1 & -1 \\ 0 & 0 & 0 \\ 1 & 1 & 1 \end{bmatrix} \quad \text{and} \quad K_y = \begin{bmatrix} -1 & 0 & 1 \\ -1 & 0 & 1 \\ -1 & 0 & 1 \end{bmatrix}.$$

The gradient magnitude  $|\nabla_P L|$  is here computed by the  $L^\infty$  norm and normalized by the maximum value of  $|\nabla_P L|$  so that it ranges over  $[0,1]$ .

2) *Computation of Image Contrast:* Let  $\mathcal{N}(x)$  be the  $w \times w$  window centered at  $x$ . The contrast of  $L$  at  $x$  is computed as:

$$\phi(x) = \begin{cases} 1 - \frac{L(x)}{\max_{y \in \mathcal{N}(x)} L(y)} & \text{if } \max_{y \in \mathcal{N}(x)} L(y) \neq 0 \\ 0 & \text{otherwise} \end{cases} \quad (4)$$

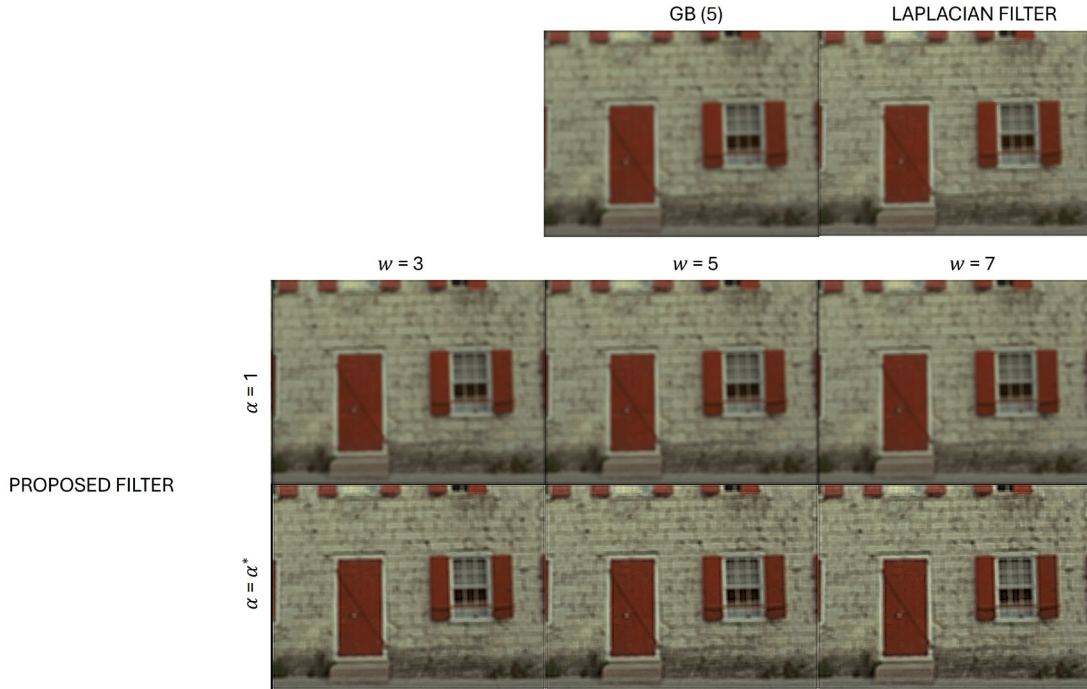


**FIGURE 6.** Laplacian and proposed sharpening applied to an image from TID-2013 (REFERENCE) distorted by Gaussian blur at two different level GB(5): the Gaussian blur is here particularly evident and both the Laplacian sharpening and the proposed approach perform poorly.

**TABLE 1.** Performance evaluation on TID-2013: the objective measures described in Section III are evaluated on the reference images (see superscript *o*), on their versions distorted by Gaussian blur (GB) at five levels (specified by the number in the brackets) and on their versions sharpened by the Laplacian filter (see superscript *I*).

Image Set	$L_m^o$	$P_m^o$	$\mu^o$	NIQE <sup>o</sup>	PSNR <sup>o</sup>	SSIM <sup>o</sup>	$L_m^I$	$P_m^I$	$\mu^I$	NIQE <sup>I</sup>	PSNR <sup>I</sup>	SSIM <sup>I</sup>
Refs	107.08	50.53	3.45	3.33	-	-	-	-	-	-	-	-
GB (1)	106.97	43.71	3.91	3.28	36.15	0.97	115.70	71.04	3.26	32.26	21.35	0.70
GB (2)	106.88	38.75	4.34	3.71	31.33	0.91	114.79	64.47	3.41	32.83	22.42	0.74
GB (3)	106.72	31.03	5.23	4.34	27.39	0.79	112.70	50.18	3.82	26.32	24.27	0.76
GB (4)	106.43	22.22	6.94	5.04	24.53	0.68	109.78	30.80	4.82	9.12	24.65	0.68
GB (5)	105.93	16.01	8.60	5.75	22.26	0.61	107.66	21.02	5.70	8.10	22.54	0.58

If  $L(x) = \max_{y \in \mathcal{N}(x)} L(y) = 0$ ,  $\phi(x)$  is set to zero.  $\phi$  varies over  $[0,1]$  and is a modified version of the Milano Retinex contrast MiRCO presented in [21] and grounded on Retinex theory [22]. The mathematical equation of MiRCO at  $x$  looks like Eq. (4), but the denominator in the ratio of Eq. (4) is replaced by a value (ranging over  $[0,1]$ ) computed from a set of intensity ratios sampled over  $n$  random paths starting from  $x$  and scanning its neighborhood. Although MiRCO provides a less noisy contrast measure than  $\phi$ , its computational complexity and execution time are much higher, making impracticable its in-built sensor implementation as well its usage in real-time applications. In this framework,  $\phi$  provides a good compromise between runtime and contrast computation performance. Moreover,  $\phi$  preserves a very important feature of MiRCO, namely its robustness to changes of light intensity: this property enables an

accurate detection of details even in low-lighted image areas.

- 3) *Estimate of c:* On blurry and/or badly lighted images, the luminance differences computed by image gradients like Prewitt's operator are usually lower than the corresponding luminance ratios computed by a contrast measure like  $\phi$ . On any edge  $x$  (i.e. pixel with  $|\nabla PL(x)| \neq 0$ ) in blurry and/or low-lighted regions,  $|\nabla PL(x)|$  is smaller than  $\phi(x)$ , i.e.

$$\rho(x) = \frac{\phi(x)}{|\nabla PL(x)|} > 1. \quad (5)$$

We note that  $\rho(x)$  depends both on the local intensity variations (captured by contrast and gradient) and on global intensity variations (captured by the maximum gradient magnitude normalizing the Prewitt gradient). Let  $R$  be the set of edges of  $L$  with  $\rho$  greater than 1 and let  $|R|$  be its cardinality. When  $R$  is empty, the

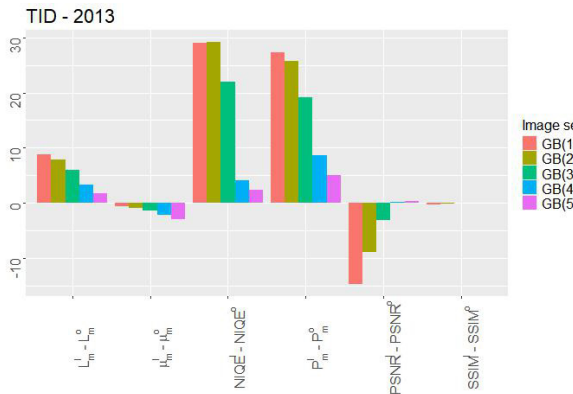


**FIGURE 7.** Graphical representation of the data in Table 1. The length of the barplot bars is equal to the difference between the performance objective measures evaluated on the images sharpened by the Laplacian filter (superscript  $l$ ) and those evaluated on the reference images (superscript  $o$ ).

**TABLE 2.** Performance evaluation of the proposed image-aware filter on TID-2013 for  $\alpha = 1$  and  $w = 3, 5, 7$ . As in Table 1, GB indicates the images modified by Gaussian blur at the levels specified in the brackets.

(a) $w = 3$						
Image Set	$L_m$	$P_m$	$\mu$	NIQE	PSNR	SSIM
GB (1)	106.03	60.32	3.78	5.48	25.99	0.82
GB (2)	106.00	55.75	3.93	5.81	26.88	0.83
GB (3)	105.96	44.08	4.39	6.02	27.76	0.80
GB (4)	105.77	27.03	5.95	4.84	25.90	0.71
GB (5)	105.15	17.60	7.58	4.43	22.70	0.60
(b) $w = 5$						
Image Set	$L_m$	$P_m$	$\mu$	NIQE	PSNR	SSIM
GB (1)	106.00	68.66	3.66	5.63	24.51	0.80
GB (2)	105.97	63.56	3.80	5.90	25.48	0.81
GB (3)	105.94	50.64	4.18	6.16	27.08	0.80
GB (4)	105.78	29.44	5.71	4.79	26.24	0.71
GB (5)	105.14	18.01	7.40	4.37	22.76	0.60
(c) $w = 7$						
Image Set	$L_m$	$P_m$	$\mu$	NIQE	PSNR	SSIM
GB (1)	106.01	74.69	3.60	5.60	23.46	0.77
GB (2)	105.96	69.36	3.72	5.84	24.43	0.79
GB (3)	105.93	55.39	4.07	6.04	26.33	0.79
GB (4)	105.80	31.56	5.54	4.84	26.42	0.72
GB (5)	105.12	18.31	7.26	4.42	22.79	0.60

method returns the input image, otherwise the image is sharpened and  $c$  is computed as

$$c = \frac{1}{|R|} \sum_{y \in R} \rho(y). \quad (6)$$

The sharpening level depends on the parameters  $c$  and  $\alpha$ . Of course, being  $\rho(x) > 1$ ,  $c$  is also greater than 1. Moreover, being the image data discrete, the value of  $c$  is upper-bounded. As discussed above, the value of  $c$  is here image-dependent and is determined by Equation (6) without any user supervision. On the contrary, the value of  $\alpha$  is an user-defined threshold. By default  $\alpha = 1$ , but this work also

**TABLE 3.** Performance evaluation of the proposed image-aware filter on TID-2013 for  $\alpha = \alpha^*$  and  $w = 3, 5, 7$ . As in Table 1, GB indicates the images modified by Gaussian blur at the levels specified in the brackets.

(a) $w = 3$						
Image Set	$L_m$	$P_m$	$\mu$	NIQE	PSNR	SSIM
GB (1)	106.12	69.16	3.63	5.46	23.85	0.79
GB (2)	106.22	70.33	3.72	6.03	23.78	0.79
GB (3)	106.39	64.42	3.96	6.25	24.05	0.77
GB (4)	106.55	42.03	5.06	5.07	24.50	0.71
GB (5)	105.94	25.09	6.60	4.21	22.15	0.59

(b) $w = 5$						
Image Set	$L_m$	$P_m$	$\mu$	NIQE	PSNR	SSIM
GB (1)	106.00	72.00	3.59	5.66	23.43	0.78
GB (2)	106.10	74.24	3.67	6.25	23.16	0.77
GB (3)	106.32	72.07	3.87	6.06	23.03	0.75
GB (4)	106.70	49.39	4.75	5.24	23.89	0.69
GB (5)	106.06	27.52	6.19	4.08	22.20	0.58

(c) $w = 7$						
Image Set	$L_m$	$P_m$	$\mu$	NIQE	PSNR	SSIM
GB (1)	105.93	72.43	3.59	5.62	23.44	0.78
GB (2)	106.02	75.16	3.66	6.28	23.08	0.77
GB (3)	106.28	76.10	3.83	5.84	22.44	0.73
GB (4)	106.79	54.26	4.65	5.37	23.32	0.68
GB (5)	106.13	29.66	5.89	4.08	22.21	0.57

proposes to set it based on the image content as follows:

$$\alpha^* = \frac{255}{\max(L * F)}. \quad (7)$$

The experiments reported in the next Sections show that this choice provides in many cases an efficacious edge enhancement.

### III. FILTER EVALUATION

The proposed filter is here evaluated on two different datasets and its performance is compared with that exploiting the standard Laplacian filter which presents a similar mathematical structure. Laplacian filter is computed on a  $3 \times 3$  window and its kernel is defined by Equation (2) with  $c = 8$ . In the following, Subsection III-A provides some details on the implementation of the proposed filter, Subsection III-B presents the datasets used for testing, Subsection III-C describes the evaluation metrics, and Subsection III-D reports and discusses the results achieved by the proposed filter, also in comparison with the Laplacian one, that - as already mentioned in the paper - presents a similar mathematical structure and can be obtained by setting  $c = 8$  in Equation (2). Nevertheless, for sake of completeness, a comparison with other three popular sharpening algorithms is presented in Appendix B.

### A. IMPLEMENTATION DETAILS

In the current implementation of the proposed filter, the luminance  $L$  of an RGB image is computed by averaging pixel-by-pixel the R, G, B image channels. To make the estimate of  $c$  more robust against image noise,  $L$  is smoothed by a  $3 \times 3$  median filter, and the set  $R$  is refined by excluding pixels with  $\rho$  very proximate to 1, i.e.  $\rho(x) > 1 + \varepsilon$ , where

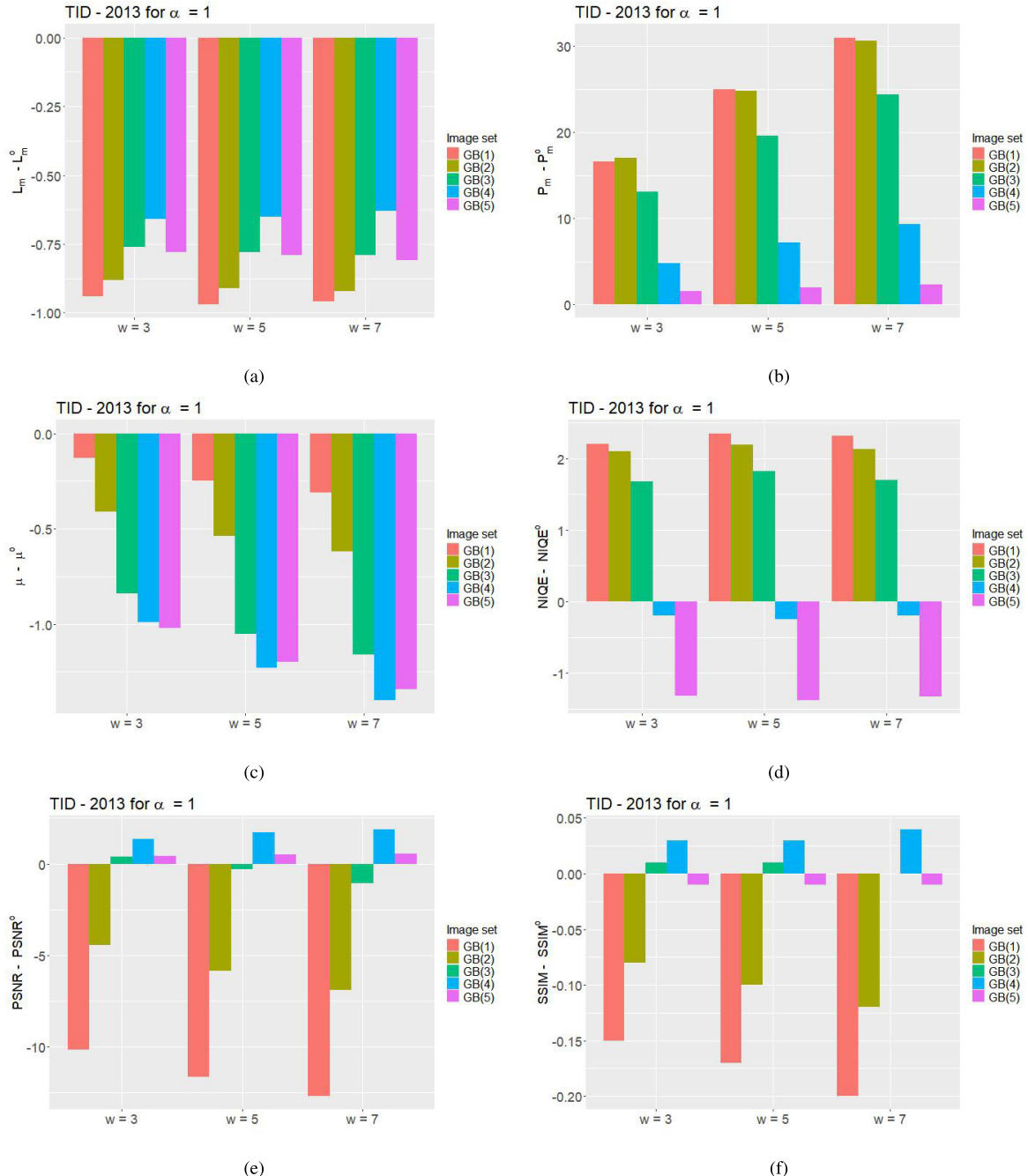


**FIGURE 8.** Graphical representation of the data in Table 2. The length of the barplot bars is equal to the difference between the performance objective measures evaluated on the images sharpened by the Laplacian-like sharpening filter and those evaluated on the images not subjected to sharpening (superscript  $o$ ). After the sharpening procedure,  $P_m$  is increased (i.e. bar height with positive value) in 100% of cases,  $\mu_m$  is decreased in 100% of cases, PSNR is increased in 53.3% of cases, and SSIM is slightly increased in 33.3% of cases.  $L_m$  is slightly decreased in all the cases, but the decrement does not exceed 1. NIQE is increased in 60% of cases, and its increment does not exceed 2.5. In the remaining 40% of cases, NIQE is reduced approximately by 1.5.

$\varepsilon = 0.05$ . In fact, due to the discrete nature of image data, for  $1 \leq \rho \leq 1.05$ ,  $\phi$  and  $|\nabla_P L(x)|$  are very close to each other. Also isolated groups of five or less pixels of  $R$  and pixels with  $\rho(x)$  exceeding the 98% percentile of the  $\rho$  distribution are discarded from the estimate of  $c$ , since they correspond likely to noise. The image  $I * K$  is then smoothed with a  $3 \times 3$  median filter and summed up to  $I$  as in Equation (1)

to diminish possible noise. All the thresholds used here have been set empirically.

## B. DATASETS

The performance of the proposed filter are evaluated here on the public datasets TID-2013 [23] and MEXICO-2020 [24].

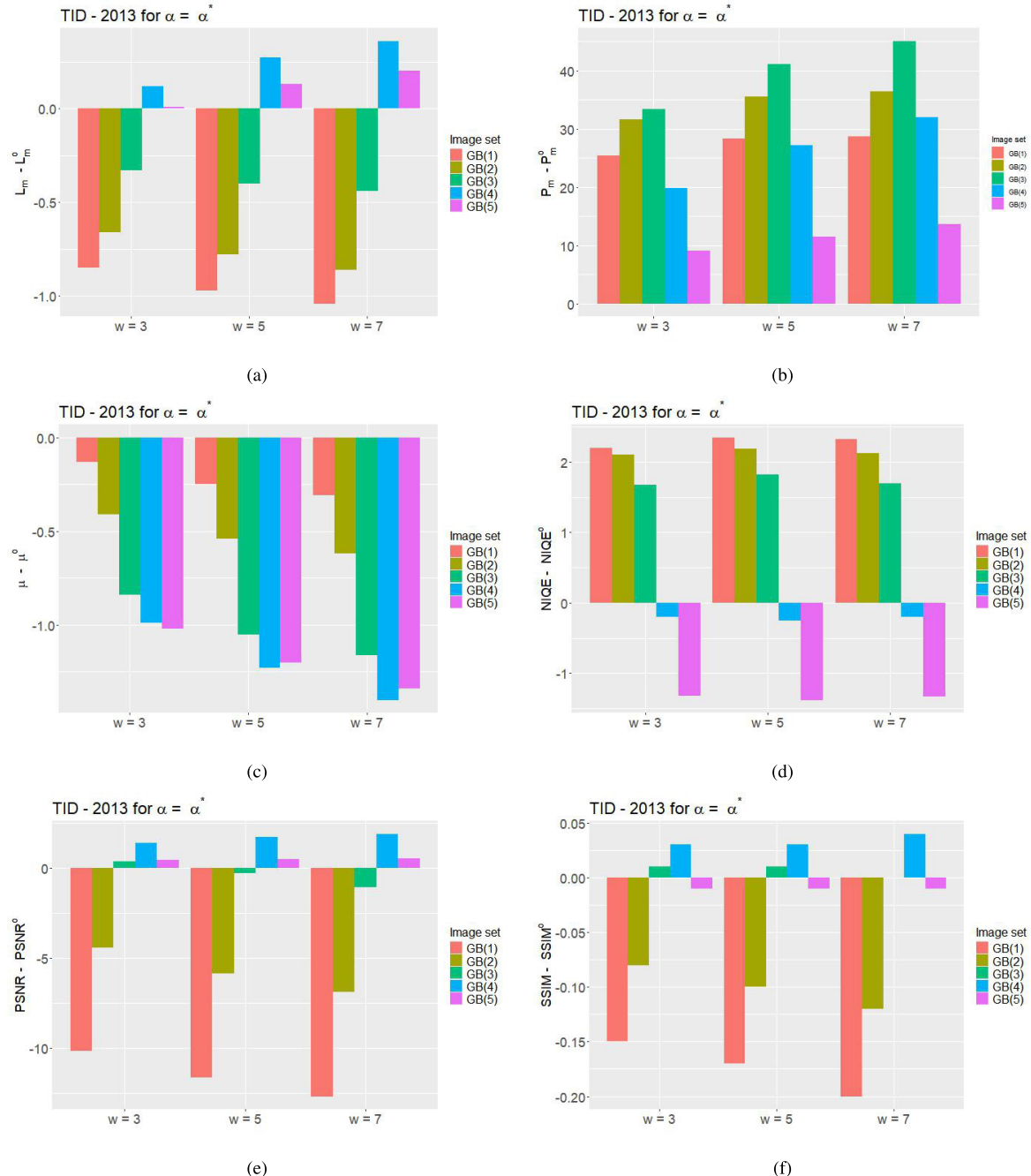


**FIGURE 9.** Graphical representation of the data in Table 3. The length of the barplot bars is equal to the difference between the performance objective measures evaluated on the images sharpened by the Laplacian-like sharpening filter and those evaluated on the images not subjected to sharpening (superscript  $o$ ). After the sharpening procedure,  $P_m$  is increased (i.e. bar height with positive value) in 100% of cases,  $\mu_m$  is decreased in 100% of cases, PSNR is slightly increased in about 47% of cases, and SSIM is slightly increased in 33.3% of cases.  $L_m$  is slightly increased in 33.3% of cases, and slightly decreased in 60% of cases, but the decrement does not exceed one and the increment does not exceed 0.5. NIQE is increased in 60% of cases, and its increment does not exceed 2.5. In the remaining 40% of cases, NIQE is reduced approximately by 1.5.

The dataset TID-2013 consists of 25 real-world, indoor and outdoor images, each of one has been synthetically modified by 24 distortions, each of which with five different levels. These distortions include noise addition, Gaussian blurring, aberration, in-painting, compression, local changes of color and contrast. The size of each image is

512 × 384 pixels. The original images are provided as reference (i.e. gold standards) and each distortion has been performed at five increasing levels, from slight to strong, as illustrated in Figure 3(a). Although the images of TID-2013 are synthetic, they are of interest because they enable to identify which distortions and levels of distortion a given

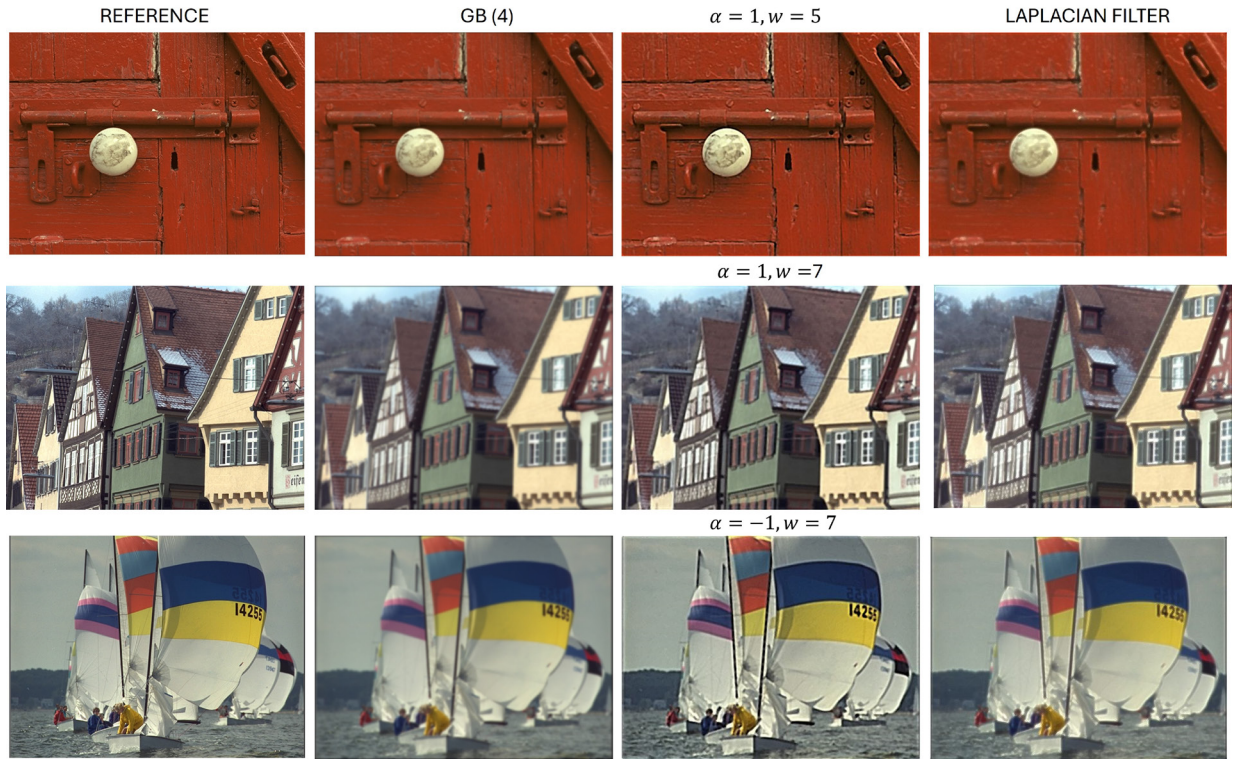


**FIGURE 10.** Three images from TID-2013 (first column), their versions distorted by Gaussian blur at level 4 (second column), their versions sharpened by the proposed filter for different values of  $\alpha$  and  $w$  (third column) and their versions processed by Laplacian sharpening (fourth column).

**TABLE 4.** Performance Evaluation on MEXICO-2020: the objective measures described in Section III are evaluated on the input images (see superscript o) and on their versions sharpened by the Laplacian filter (see superscript l).

T[ms]	$L_m^o$	$P_m^o$	$\mu^o$	NIQE <sup>o</sup>	$L_m^l$	$P_m^l$	$\mu^l$	NIQE <sup>l</sup>
15	34.28	10.59	4.39	4.64	36.23	18.89	3.26	11.69
18	46.57	14.26	4.81	4.28	49.32	24.83	3.42	14.10
21	58.35	17.57	5.10	4.07	61.77	29.85	3.51	17.16
24	69.88	20.58	5.25	3.90	73.85	34.06	3.56	19.64
27	80.95	23.19	5.39	3.83	85.29	37.24	3.62	19.82

**TABLE 5.** Performance Evaluation of the proposed sharpening on MEXICO-2020 for  $\alpha = 1$  and different values of  $w$ .

T[ms]	$w = 3$				$w = 5$				$w = 7$			
	$L_m$	$P_m$	$\mu$	NIQE	$L_m$	$P_m$	$\mu$	NIQE	$L_m$	$P_m$	$\mu$	NIQE
15	33.08	16.57	3.76	4.64	33.07	19.76	3.61	4.62	33.08	22.11	3.56	4.73
18	45.37	21.62	4.00	4.52	45.36	25.79	3.82	4.33	45.37	29.13	3.74	4.45
21	57.12	25.84	4.14	4.42	57.10	30.61	3.92	4.19	57.09	34.61	3.81	4.45
24	68.66	29.51	4.23	4.31	68.60	34.89	3.98	4.24	68.58	39.27	3.86	4.34
27	79.70	32.43	4.32	4.28	79.61	38.21	4.05	4.21	79.56	42.74	3.91	4.17

**TABLE 6.** Performance evaluation of the proposed sharpening on MEXICO-2020 for  $\alpha = \alpha^*$  and different values of  $w$ .

T[ms]	$w = 3$				$w = 5$				$w = 7$			
	$L_m$	$P_m$	$\mu$	NIQE	$L_m$	$P_m$	$\mu$	NIQE	$L_m$	$P_m$	$\mu$	NIQE
15	33.28	23.65	3.56	4.83	33.31	26.49	3.50	4.82	633.34	28.24	3.46	5.07
18	45.55	28.27	3.74	4.45	45.55	32.00	3.66	4.68	45.57	33.72	3.63	4.70
21	57.26	31.87	3.87	4.48	57.25	35.71	3.78	4.39	57.24	37.77	3.74	4.54
24	68.77	35.03	3.99	4.26	68.72	39.21	3.86	4.21	68.69	44.50	3.81	4.43
27	79.77	37.15	4.09	4.21	79.69	41.45	3.94	4.15	79.63	43.39	3.89	4.21

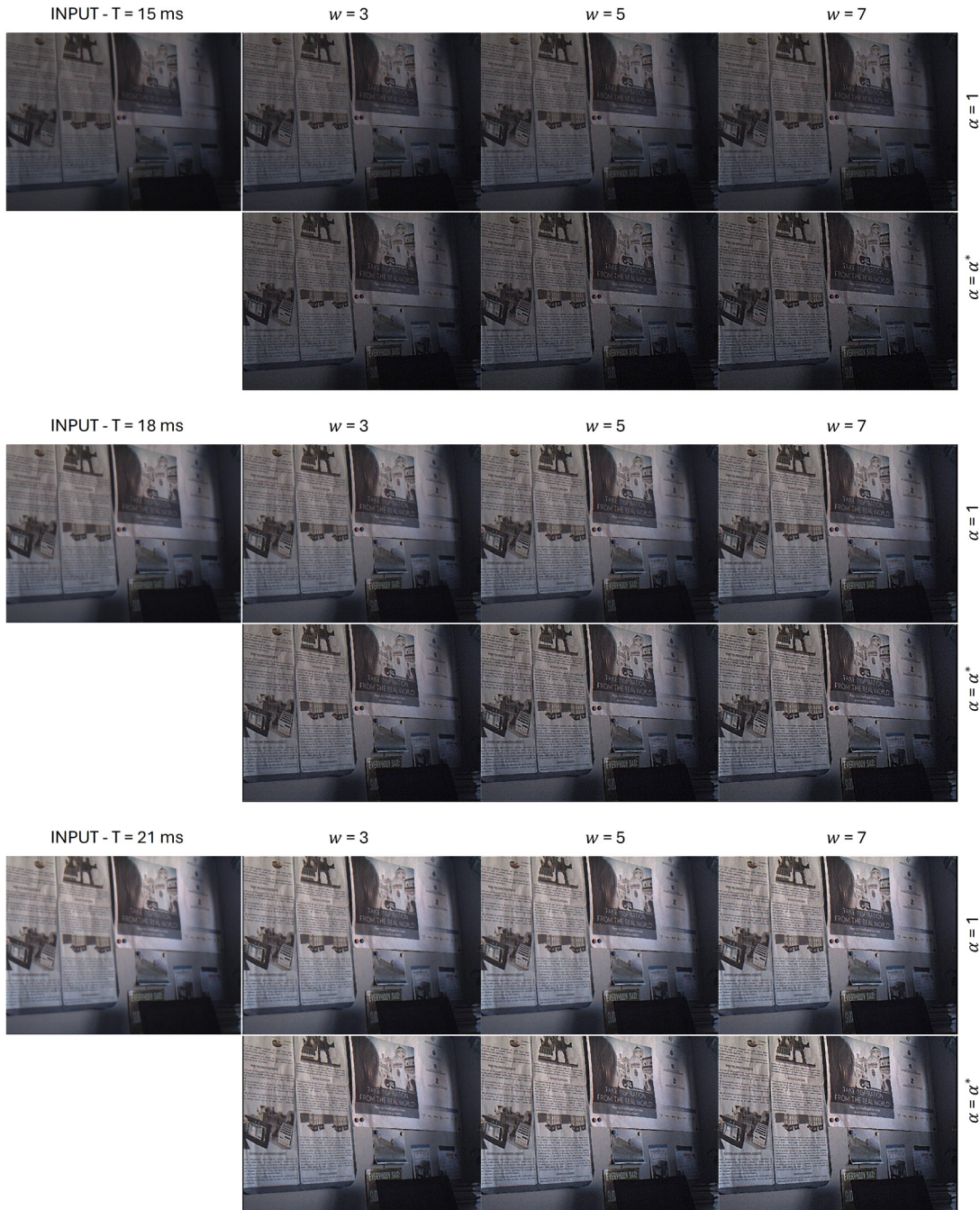


**FIGURE 11.** Results of the proposed sharpening on an image from MEXICO-2020 with  $T = 15, 18, 21$  ms. Different values of  $\alpha$  and  $w$  have been used.

algorithm is capable of correcting. Indeed, synthetic datasets offer higher model accuracy [25], [26] and thus for this particular purpose to identify types and levels of distortion they prove to be more suitable than a dataset of real data. The proposed sharpening filter is here tested on the 125 images distorted by Gaussian blur that typically affects the edge quality and can be reduced by sharpening. Appendix B reports additional experiments where the proposed filter has

been applied to JPEG and JPEG2000 compressed images from TID-2013 with results similar to those described in this Section.

The dataset MEXICO-2020 consists of 50 real-world scenes of indoor and outdoor environments acquired by the FLIR camera FMVU-03MTM-CS under six exposure times  $T = 6, 15, 18, 21, 24, 27$  ms for simulating different levels of light intensity: the lower the illumination intensity the

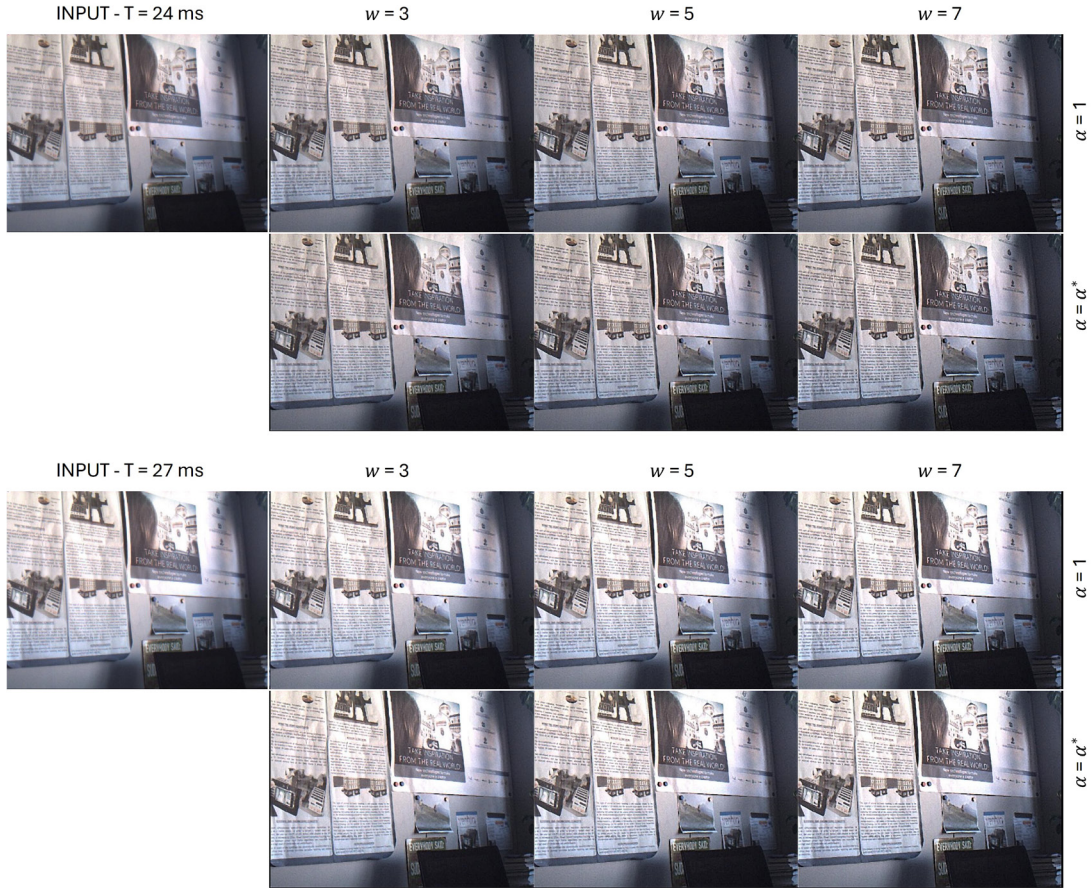


**FIGURE 12.** Results of the proposed sharpening on an image from MEXICO-2020 with  $T = 24$  and  $27$  ms. Different values of  $\alpha$  and  $w$  have been used.

**TABLE 7.** Performance Evaluation of the proposed sharpening on the aerial images from the Kaggle repository test in [46].

$(\alpha, w)$	$L_m$	$P_m$	$\mu$	NIQE
Input	98.59	31.25	4.77	4.22
$(\alpha = 1, w = 3)$	97.54	39.03	4.69	5.18
$(\alpha = 1, w = 5)$	97.58	43.22	4.52	5.15
$(\alpha = 1, w = 7)$	97.62	46.47	4.42	5.14
$(\alpha = \alpha^*, w = 3)$	97.85	49.60	4.38	5.27
$(\alpha = \alpha^*, w = 5)$	97.90	54.26	4.27	5.31
$(\alpha = \alpha^*, w = 7)$	97.90	56.91	4.21	5.44

lower the edge visibility and sharpness. In this work,  $T = 6$  ms was not considered since the images acquired with this exposure time are too dark and sharpening cannot be visually appreciated. The total number of images from MEXICO-2020 considered here is thus 250. The size of each image from MEXICO-2020 is  $640 \times 480$  pixels. As shown in Figure 3(b), the visibility and sharpness of the image edges is scarce for  $T = 15$  ms and increases with  $T$ . Like the multiple distortion levels of TID-2013, the multiple-exposure data of MEXICO-2020 enables testing the sharpening filter on images with different quality.

### C. METRICS

The performance of the proposed filter has been evaluated by comparing the following features before and after sharpening: the image luminance ( $L_m$ ), its (not normalized) Prewitt's gradient magnitudes ( $P_m$ ), the no-reference sharpness metric in [27] ( $\mu$ ) basically measuring the edge thickness, and the image regularity measure in [28] (NIQE). All these measures are related to human perception of image quality. For the dataset TID-2013, that includes references (i.e. not distorted) images, the values of PSNR (peak-signal-to-noise-ratio) and SSIM (structural similarity index) are also computed.

To be effective, a sharpening algorithm is expected to change these features as follows. After sharpening,  $P_m$  and  $\mu$  should respectively increase and decrease, meaning that the edge visibility is improved, while  $L_m$  and NIQE should remain almost stable because the increment of edge magnitude should not significantly change the global luminance and not introduce local irregularities worsening the image naturalness. Finally, the higher the image quality, the higher the values of PSNR and SSIM. Differently from the other measures considered here, PSNR and SSIM are full reference metrics, thus their value

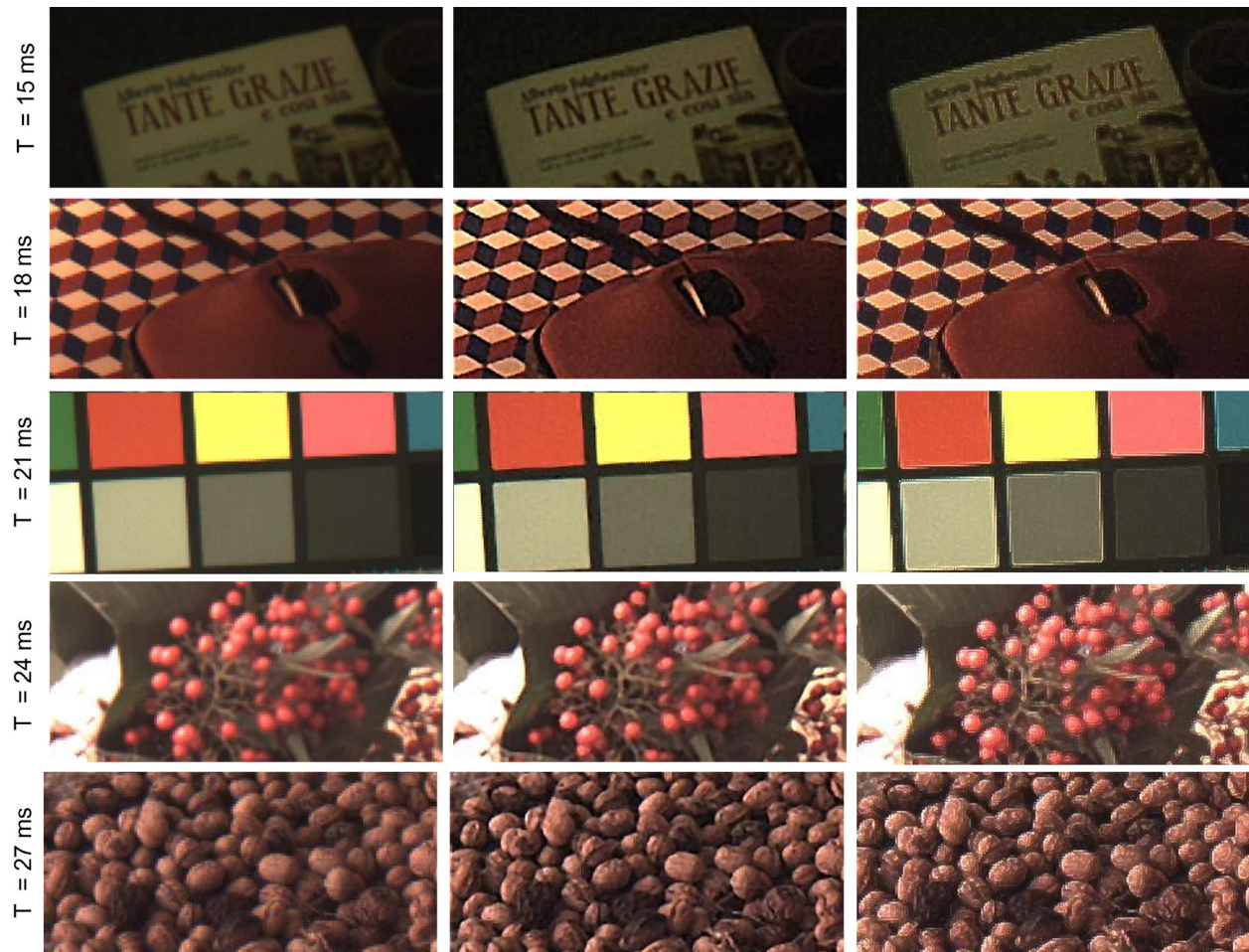


**FIGURE 13.** Particulars of some images from MEXICO-2020 and their versions sharpened by the proposed filter for  $\alpha = 1$  and  $w = 3$ , and by a Laplacian one.

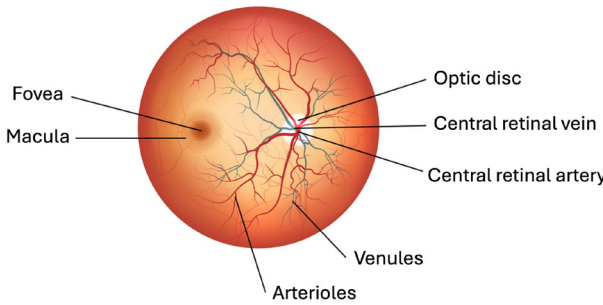


**FIGURE 14.** In adult humans, the retina includes approximately 7 million cones and 75 to 150 million rods. The optic disc, a region of the retina also known as “the blind spot” because it lacks photoreceptors, is positioned near the optic papilla, where the optic nerve fibres exit the eye. It appears as a  $3 \text{ mm}^2$  oval-shaped white spot. The macula is located temporally (towards the temples) to this disc, and its centre is the fovea, a pit that is responsible for acute central vision but is less sensitive to light due to a lack of rods.

depends on the reference defined as gold-standard. This is an important point, that will be discussed in more details in Subsection III-D.

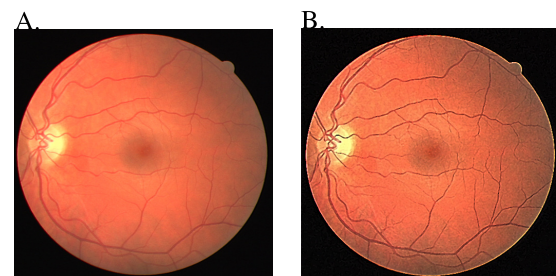


**FIGURE 15.** A. Original image of the retina. B. Processed image. The image processed through the sharpening filter shows in significantly greater detail than the original the blood vessels along their entire length, greater edge accuracy of the fovea area and of the optic disc.

#### D. RESULTS

Table 1 shows the evaluation measures (averaged over the number of test images) computed on the original images of TID-2013 (see the superscript  $o$ ) and on its versions sharpened by the Laplacian filter (see the superscript  $l$ ). Tables 2 and 3 show the corresponding mean evaluation measures computed on the images sharpened by the proposed

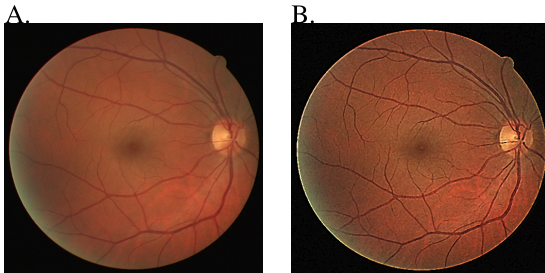


**FIGURE 16.** A. Original image of the retina. B. Processed image. Even in low light conditions, the image processed through the sharpening filter shows in significantly greater detail than the original the blood vessels along their entire length, greater edge accuracy of the fovea area and of the optic disc.

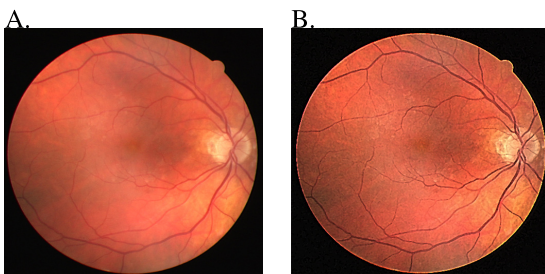


**FIGURE 17.** A. Original image of the retina. B. Processed image. The image processed through the sharpening filter shows in significantly greater detail than the original the blood vessels along their entire length, greater edge accuracy of the darker areas of the ocular fundus and the edges of the optic disc. On retinal endoscopy of a healthy eye, the area of the macula should appear as a well-defined area. If, however, a darker, opaque, or irregularly shaped area is observed (as in this image), it could be a sign of a pathologic condition that impairs the function of the macula.

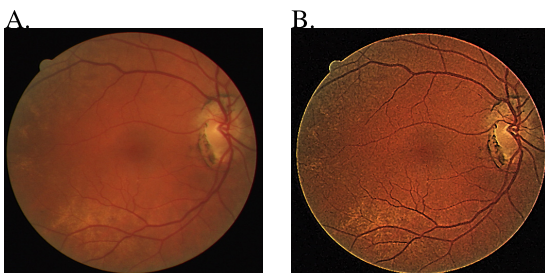


**FIGURE 18.** A. Original image of the retina. B. Processed image. The image processed through the sharpening filter shows in significantly greater detail than the original. In particular, black pigmentation areas around the optic disk are shown in greater resolution, and suggest the need of further analyses to assess a possible diagnosis of optic disc melanocytoma, a rare form of cancer that while generally considered benign, it can occasionally grow or cause visual problems [36].

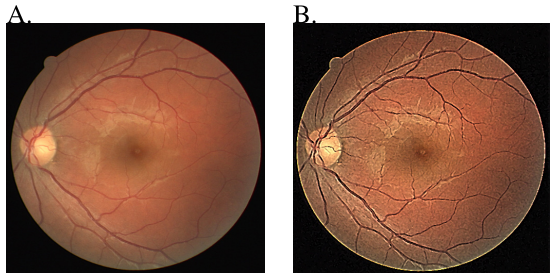


**FIGURE 19.** A. Original image of the retina. B. Processed image. The image processed through the sharpening filter shows in significantly greater detail than the original. In particular, we notice in higher resolution whitish areas around the fovea and (although smaller in size) also in the macula. The better view of these regions can help the doctor in evaluating a possible diagnosis of macular pucker, that is a condition characterized by the formation of scar tissue on the macula's surface, the central area of the retina that is essential for clear, detailed vision. This scar tissue may create wrinkles or pockers on the macula, resulting in unclear or distorted central vision [37]. With the help of increased resolution, the image can also be used as part of differential diagnosis that also assesses the possibility that it is white dot fovea, a condition characterized by the presence of small, white dots on the surface of the fovea [38].

proposed Laplacian-like sharpening filter and those evaluated on the reference images (superscript  $o$ ) are shown. Similar figures, which refer to the data obtained from JPEG and JPEG2000 compressed images, are provided in Appendix B to illustrate the numerical data in Tables 10, 11, and 12 (see Figures 33, 34, 35, 40, and 41). Referring the reader to the captions of each of these figures for a more detailed description, the results obtained in the validation experiments of the proposed filter state that, in a proportion of cases ranging from 73.3% to 100%,  $\mu$  undergoes a significant reduction, and  $P_m$  undergoes a marked increment in 100% of cases.

As shown in Figure 3 (a), the visual quality of the original images decreases by increasing the distortion level. This behavior is clearly described by the numerical measures. In fact, while  $L_m$  remains more or less stable,  $P_m$  and  $\mu$  respectively increases and decreases, meaning that edges are improved; NIQE increases denoting a loss of image regularity and naturalness; finally, PSNR and SSIM become smaller since the higher the distortion level, the higher the difference between the distorted image and the reference.

The Laplacian sharpening remarkably increases  $P_m$  and decreases  $\mu$  with respect to the corresponding original values, but over-enhances the edges making the image unnatural, noisy and far from the reference one, as inferable from the high values of  $L_m$  and NIQE and from the small ones of PSNR and SSIM. In particular, since the Laplacian sharpened image becomes brighter, the edges appear poorly improved, as illustrated by the examples in Figures 4, 5, 6, 10.

The proposed filter performs much better: for any value of  $\alpha$  and  $w$ , the edges are magnified, the luminance is more or less stable and NIQE is only slightly increased, meaning that the image naturalness is much better preserved. However, for the both the filters, the higher the distortion

filter with different values of the parameters  $\alpha$  and  $w$ . In order to facilitate comparisons of the results shown in Tables 1, 2 and 3, Figures 7, 8, and 9 are provided. Figure 7 shows the barplots of the differences between the performance objective measures evaluated on the images sharpened by the proposed Laplacian sharpening filter (superscript  $l$ ) and those evaluated on the reference images (superscript  $o$ ). In Figures 8 and 9 the barplots of the differences between the performance objective measures evaluated on the images sharpened by the



**FIGURE 20.** Results of the proposed sharpening on three remote sensing images showing natural and artificial structures from [39].

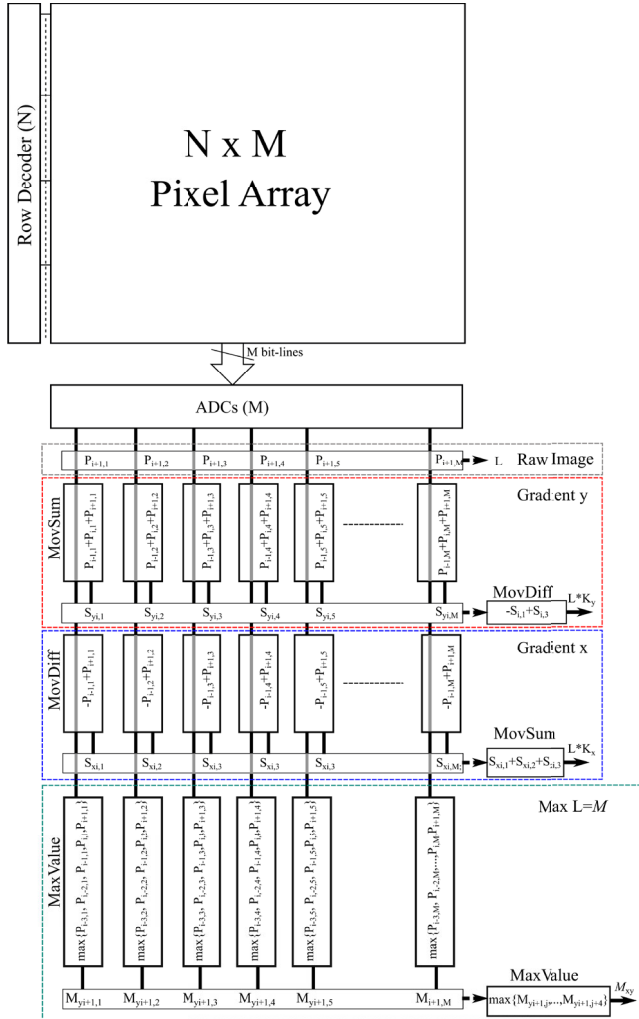


**FIGURE 21.** Digital block used to compute the components of the Prewitt's Gradient along  $y$  during the image readout. Four memories are needed to store the pixel values of the same  $j$ -th column that are progressively read out and converted by the  $j$ -th ADCs. The circuits calculate the elements of  $L * K_y$  through a 3 terms moving sum. Here  $M_{xy}$  is the maximum value of  $L$  at the position  $(x, y)$ .

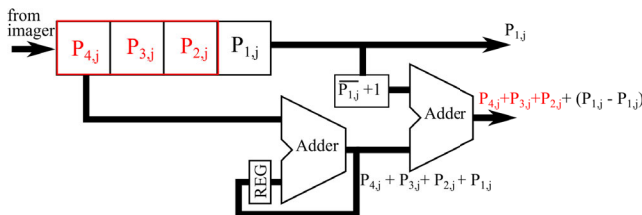


**FIGURE 22.** The block MovSum used to implement the computation of the Prewitt's gradient during the image readout. Four memories are needed to store the pixel values of the same  $j$ -th column that are progressively read out and converted by the  $j$ -th ADCs. It calculates the elements of  $K_y$  along the vertical direction through a 3 terms moving sum. To implement the moving sum, the rightmost term ( $P_{1,j}$ ) must be always subtracted from the output of the first adder.

level, the lower improvement of edge and image quality is. In general, the proposed filter achieves very good results on any blur level from 1 to 4, but - as well as the Laplacian

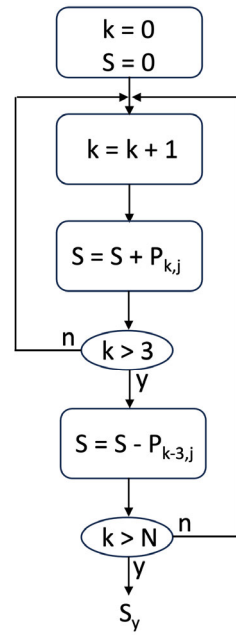


**FIGURE 23.** Flowchart for the MovSum block organized in an array of  $M$  elements in the first processing layer (Gradienty).

sharpening - it performs poorly on GB(5), where the Gaussian blur is particularly evident. From Tables 2 and 3 it comes out that the edge magnitude increases with  $\alpha$  and  $w$  and is particularly high for  $\alpha = \alpha^*$ . In fact,  $\alpha^*$  is often greater than 1 and this increases the contribution of the sharpened luminance in Equation (1). Moreover, the higher  $w$ , the higher the value of  $\phi(x)$ , thus the higher the value of  $\rho(x)$  and  $c$  and more evident the sharpening is: in fact, in the most real world images, in a small neighborhood of  $x$ , the variability of the luminance  $L(x)$  is low, thus  $\rho(x)$  is close to 1, making the sharpening effect negligible or even null ( $R$  is empty). On the contrary, the higher  $w$ , the higher the variability of  $L(x)$  and the higher the probability of finding  $\phi(x) < 1$  is (of course, the final result depends on the local luminance distribution).

It is to note that in some cases, the Laplacian sharpening and the proposed one reach a level of edge visibility much higher than that of the reference (see for instance the values  $P_m$  and  $\mu$  for GB(1) and GB(2)). Since this effect makes the sharpened image and the reference different, the values of PSNR and SSIM decrease. Nevertheless, such a decrement does not indicate a worsened quality of the sharpened images: indeed, a visual inspection of the results confirms that the edges have a better visibility after sharpening, also in comparison with the reference: as mentioned in Section III-C, PSNR and SSIM depend on the reference, but in this case even the reference edges can be improved.

Tables 4, 5 and 6 report the evaluation measures computed on the original images of MEXICO-2020 and on their versions sharpened by using the Laplacian filter and the

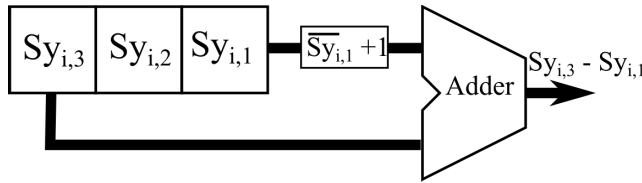


**FIGURE 24.** The block MovDiff used to implement the Prewitt's Gradient during the image readout. It consists of a 3-stages shift-register storing three  $S_y$  term that are progressively fed during the readout. For each new data shift, it calculates the difference between the first and the third term ( $-S_{y,i,j} + S_{y,i,j+2}$ ).

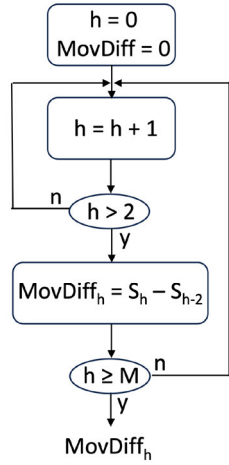


**FIGURE 25.** Flowchart for the MovDiff block organized in an array of  $M$  elements in the second processing layer (*Gradientx*).

proposed one with different parameter values. As for TID-2013, these values are averaged over the number of test images. It is to note that although the quality of the original images of MEXICO-2020 increases with  $T$ , the corresponding value of  $\mu$  increases with  $T$  (see Table 4). As a better quality should correspond to a better edge visibility, this behavior could appear surprising but actually it is not because of the noise that usually affects badly lighted images. In fact, low light images are characterized by brightly colored pixels scattered throughout the image and due to physical limitation of the acquisition device. These noisy pixels produce narrow edges that, having a small width, diminish the value of  $\mu$  with respect to a well illuminated image, because, unfortunately, any sharpening filter will tend to emphasize not only important edges but also such noise. Anyway, the performance of the proposed sharpening filter on MEXICO-2020 are like expected:  $P_m$  increases,  $\mu$  decreases and  $L_m$  is stable with respect to their original values, while NIQE remains stable for  $T = 15$  and increases slightly for the other values of  $T$ . Like for TID-2013, the higher  $\alpha^*$  and  $w$ , the stronger the enhancement effect (see Figures 11 and 12 for an example), and the Laplacian sharpening is much stronger than that provided by the proposed filter. In particular, the Laplacian-filtered images exhibit higher values of  $L_m$ ,  $P_m$  and NIQE and lower values of  $\mu$  than the proposed filter.

**TABLE 8.** Operations for the block MovSum implementing a three-tap moving sum, which is used to calculate the moving sum used to build the gradient magnitude in (3). During the image readout (Fig.21), for each column the values of the pixels are added together, as the rows are selected and converted by the ADCs, while the fourth pixel is subtracted.

Row	M0	M1	M2	M3	Sum
1	$P_{1,j}$	0	0	0	$P_{1,j} - 0$
2	$P_{2,j}$	$P_{1,j}$	0	0	$P_{2,j} + P_{1,j} - 0$
3	$P_{3,j}$	$P_{2,j}$	$P_{1,j}$	0	$P_{3,j} + P_{2,j} + P_{1,j} - 0$
4	$P_{4,j}$	$P_{3,j}$	$P_{2,j}$	$P_{1,j}$	$P_{4,j} + P_{3,j} + P_{2,j} + (P_{1,j} - P_{1,j})$
5	$P_{5,j}$	$P_{4,j}$	$P_{3,j}$	$P_{2,j}$	$P_{5,j} + P_{4,j} + P_{3,j} + (P_{2,j} - P_{2,j})$
6	$P_{6,j}$	$P_{5,j}$	$P_{4,j}$	$P_{3,j}$	$P_{6,j} + P_{5,j} + P_{4,j} + (P_{3,j} - P_{3,j})$
...	...	...	...	...	...
n	$P_{n,j}$	$P_{n-1,j}$	$P_{n-2,j}$	$P_{n-3,j}$	$P_{n,j} + P_{n-1,j} + P_{n-2,j}$

Both for TID-2013 and MEXICO-2020, the results have been visually inspected by three volunteers with the aim of checking and interpreting the numerical assessment. The volunteers confirmed that the proposed sharpening is less aggressive than the Laplacian one, as indicated by the higher value of PSNR and the lower value of NIQE. In particular, in the Laplacian sharpened images, the volunteers observed saturated pixels along the object borders, which have been described as shredded (see Figure 13). These artifacts become more frequent as  $T$  increases since, being image-blind, the Laplacian sharpening over-enhances already clear details. Such an effect is absent in the images sharpened by the proposed filter for  $\alpha = 1$  and  $w = 3$ , while is observable in some images for higher values of  $w$ , as well as for  $\alpha = \alpha^*$ , meaning that for the low light images of MEXICO-2020 a local, gentle edge processing (as that obtained for  $\alpha = 1$  and  $w = 3$ ) suffices for improving the detail visibility and does not generate artifacts.

To conclude, taking into account both the quantitative analysis and the visual check of the results, on both the databases TID-2013 and MEXICO-2020, the proposed image-aware sharpening filter performs well and generally results to be more accurate than that based on the Laplacian filter.

#### IV. AN APPLICATION TO RETINAL IMAGES

In modern medicine, medical imaging has become an increasingly vital tool, significantly enhancing the precision and efficiency of early disease diagnosis and treatment through direct visualization of internal organs. Sharp and precise images are critical for proper diagnosis. Indeed, as long as the image is accurate, the doctor can discriminate between diseases that may be confused with one another from an inaccurate image or generic symptoms. Furthermore low-quality images pose a challenge not only for the doctors' clinical diagnosis but also for computer-assisted diagnosis systems, yet obtaining high-resolution medical images frequently necessitates specialized and expensive equipment.

Based on these considerations, by way of example the results of applying our image sharpening filter on retinal images are shown here. Many disorders, including as diabetic retinopathy [29], glaucoma [30], and age-related macular

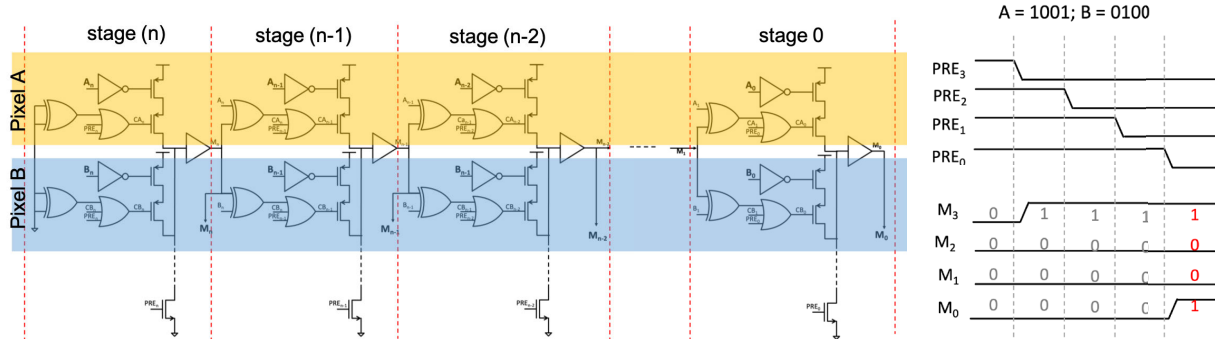


**FIGURE 26.** MaxValue block which is used find the maximum value among pixels. In this simple case, the input pixels are A and B, but multiple pixels can be put in competition by simply adding them in parallel, thanks to the modularity of the circuit. The comparison starts from the stage n (MSB) and propagates asynchronously to the last stage (LSB). The output of the network is  $M_n$ . The output bit-line are pre-charged at the same time and released with a delay( $PRE_n, PRE_{n-1}, \dots, PRE_0$ ) taking into account the propagation delay of each comparison stage. The timing diagram on the right shows how the network works when comparing two 4-bits pixels A and B, with  $A > B$ . Initially, the network is under reset, with all the pre-charge inputs asserted ( $PRE_i = H$  for  $i = 0:3$ ) and the outputs  $M_3 \dots M_0 = 0$ . The comparison starts first setting  $PRE_3 = H$ . Since  $A_3 > B_3$ , the pixel A takes the control of the first stage of the network (stage 3), writing its value  $A_3 = M_3 = 1$  and disabling the successive stages associated to the pixel B. In this simple case, the other output bits ( $M_2, M_1, M_0$ ) are controlled by pixel A. Since the comparison is an asynchronous process, the precharge signals ( $PRE_n, \dots, PRE_0$ ) must be progressively activated with a proper delay to take into account the analog delay of each stage, as shown in the timing diagram.

**TABLE 9.** Comparison of electrical performance of this work with the sensor in [44], assuming the same technology, pixel array, frame rate and supply voltages.

Parameter	Sensor [45]	This work
Technology	CMOS 110 nm	CMOS 110 nm
Pixel array	640 x 480	640 x 480
Supply voltage	3.3V/1.2V	3.3V/1.2V
Frame rate	8 fps	8 fps
Processed image	160 x 120	160 x 120
Embedded memory	365 kb	30 kb
Average power consumption for processing	$344 \mu W^1$	$28 \mu W$
Power consumption for processing and image delivering	$1.35 mW^2$	$4.28 mW^3$

<sup>1</sup> The sensor average power consumption includes QQVGA ADC conversion and on-chip processing, without the data delivering.

<sup>2</sup> The sensor average power consumption includes VGA ADC conversion and image delivering. The power consumption for VGA image dispatching is approximated to 1 mW.

<sup>3</sup> The sensor average power consumption for data delivering includes QQVGA ADC conversion and  $L, L * K_y, L * K_x$  and  $M$ . Assuming that 1 mW is required to deliver a VGA image, the same power budget can be approximated to deliver four QQVGA images.

degeneration [31], [32], can be screened for and diagnosed using retinal imaging. These conditions frequently result in anomalies in the optic disc, cup, and blood vessels. The optic disc profile and microscopic blood vessels can only be clearly seen in high-quality retinal pictures.

Both computer-aided diagnosis methods and ophthalmologists' clinical diagnosis are hampered by unsatisfactory retinal images quality [33]. In retinal images even more than in other types of medical images, in spite of the current advancements, low-quality images can still occur due to factors like poor focus, inadequate illumination, or patient issues (e.g. patient movement during image capture, presence of cataracts, corneal oedema, or vitreous haemorrhage can hinder the image quality, but also structural issues such as the spherical shape of the eye and the structure of the retina itself can also contribute to image distortion). Of crucial importance is particularly the clear view of the

anatomical structures of the retina, such as those shown in Figure 14.

The proposed sharpening filter has been applied to the retinal images available in the Kaggle Retina Blood Vessel Segmentation dataset [34]. This dataset contains a collection of 100 retinal fundus images (with size  $512 \times 512$  pixels) annotated for blood vessel segmentation. The examination of blood vessels is essential in ophthalmology since it supports the early identification and treatment of different retinal disorders, including diabetic retinopathy and macular degeneration [35]. This use case is particularly illustrative of the capabilities of our filter to significantly increase the accuracy of images, given the minimal thickness of the blood vessels in the retina and the not rare eventuality that their resolution can be easily compromised by events independent of the quality of the instrument with which the images were taken, such as (in addition to those already listed above) the

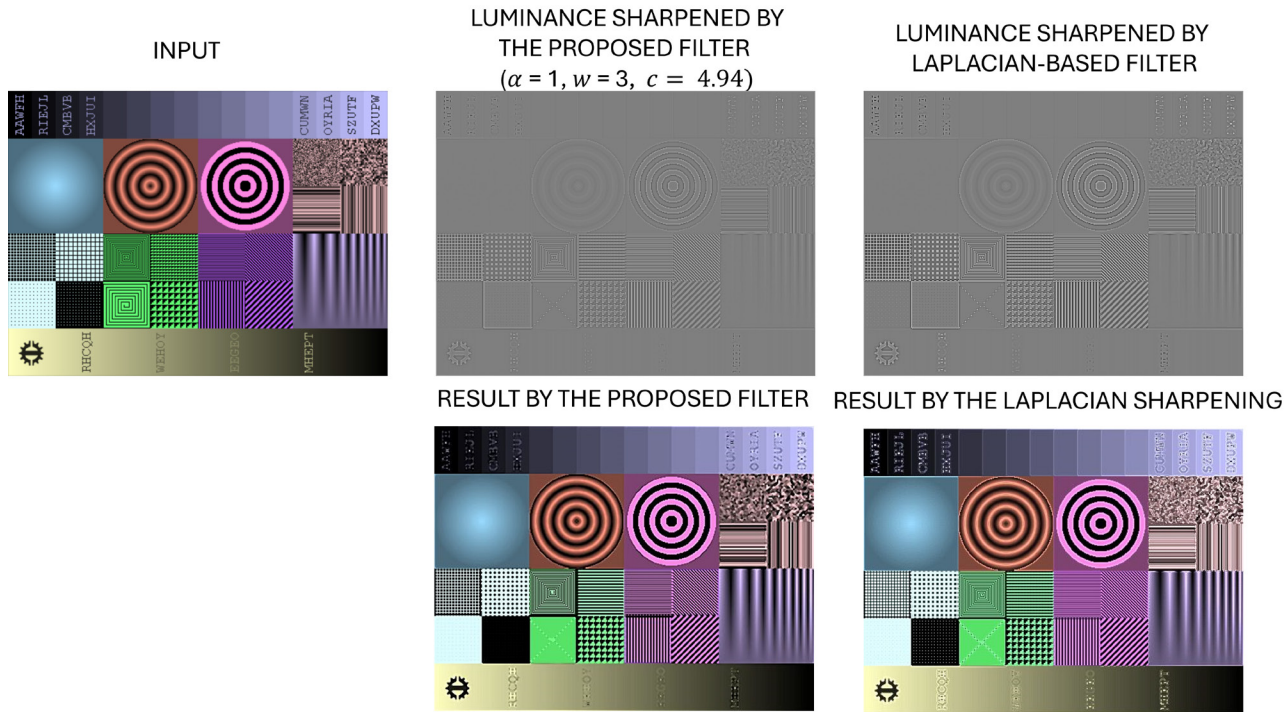


**FIGURE 27.** On top, an RGB image from TID-2013 GB(1), the sharpened versions  $K_F * L$  and  $-K_L * L$  of its luminance  $L$ : on bottom, the corresponding sharpened RGB versions. The overall brightness of  $K_F * L$  is lower than that  $-K_L * L$  because the value of  $c$  here is 4.94. Anyway, the edges (i.e. zero cross points) in  $K_F * L$  and  $-K_L * L$  are the same.

proximity to or inclusion of the vessels in other anatomical structures.

The images in Figures 15, 16, 17, 18 and 19 show the improvement immediately visible even at a visual inspection of the image quality, even in low light conditions (see Figure 16). Of potential interest to the task discussed here are the images in Figures 18 and 19 that may suggest possible retinal pathology and thus further analysis to refute or confirm diagnostic hypotheses. In the captions of each figure, the reader will find a detailed description of the case studies considered here.

## V. A DRAFT ARCHITECTURE FOR ON-CHIP IMPLEMENTATION OF THE FILTER

Embedding sensing and processing on the same chip can bring several benefits in terms of low power consumption and real-time processing, compared to a standard approach, where the computation is the prerogative of the processor. Many contributions have been published targeting on-chip image processing to enhance the performance of vision systems for specific applications. Some works adopted pixel-level processing [40], [41], [42], while others locate the processing in the periphery of the image sensor [43], [44], [45]. The best sensor architectural approach depends on the image processing that must be embedded on-chip for the specific task.

This Section presents a draft architecture for implementing the main computational blocks of the proposed filter on-chip

with the image sensor. Such an on-chip integration could be beneficial for remote sensing applications and aerial images acquisition, especially in case of sensors with constraints on power consumption, like e.g. uncrewed aerial vehicles. These images are captured by satellites and drones to monitor and/or classify geographical regions, like urban environments, forests, water bodies, farming, and are often affected by blur caused for instance by satellite or drone instability, bad weather conditions like foggy or rain, atmospheric pollution. In this case, the image details appear poorly visible and scarcely interpretable and sharpening represents a solution to mitigate these effects. By this way, Table 7 reports the evaluation measures computed on 100 aerial images with size  $100 \times 100$  pixels available in the repository *test* in [46]: these results show that the proposed sharpening effectively improves the image quality (see Figure 20 for some examples).

The low complexity of the proposed sharpening algorithm makes it possible for it to be partially integrated on-chip, together with the image sensor. In the architecture proposed here, the integration regards the computation of  $L * K_x$ ,  $L * K_y$  and the local maximum  $M$  with  $M(x) = \max\{L(y) : y \in \mathcal{N}(x)\}$  (i.e. the denominator in Equation (4)), while the computations of  $c$ ,  $\alpha$ ,  $\phi$  and Equation (1) are delegated to an external processor. This is because the computation of  $L * K_x$ ,  $L * K_y$ ,  $M$  exploit sum, subtraction and comparison operators that can be efficiently implemented on-silicon, while the computations of  $c$ ,  $\alpha$  and  $\phi$  perform pixel-wise divisions,

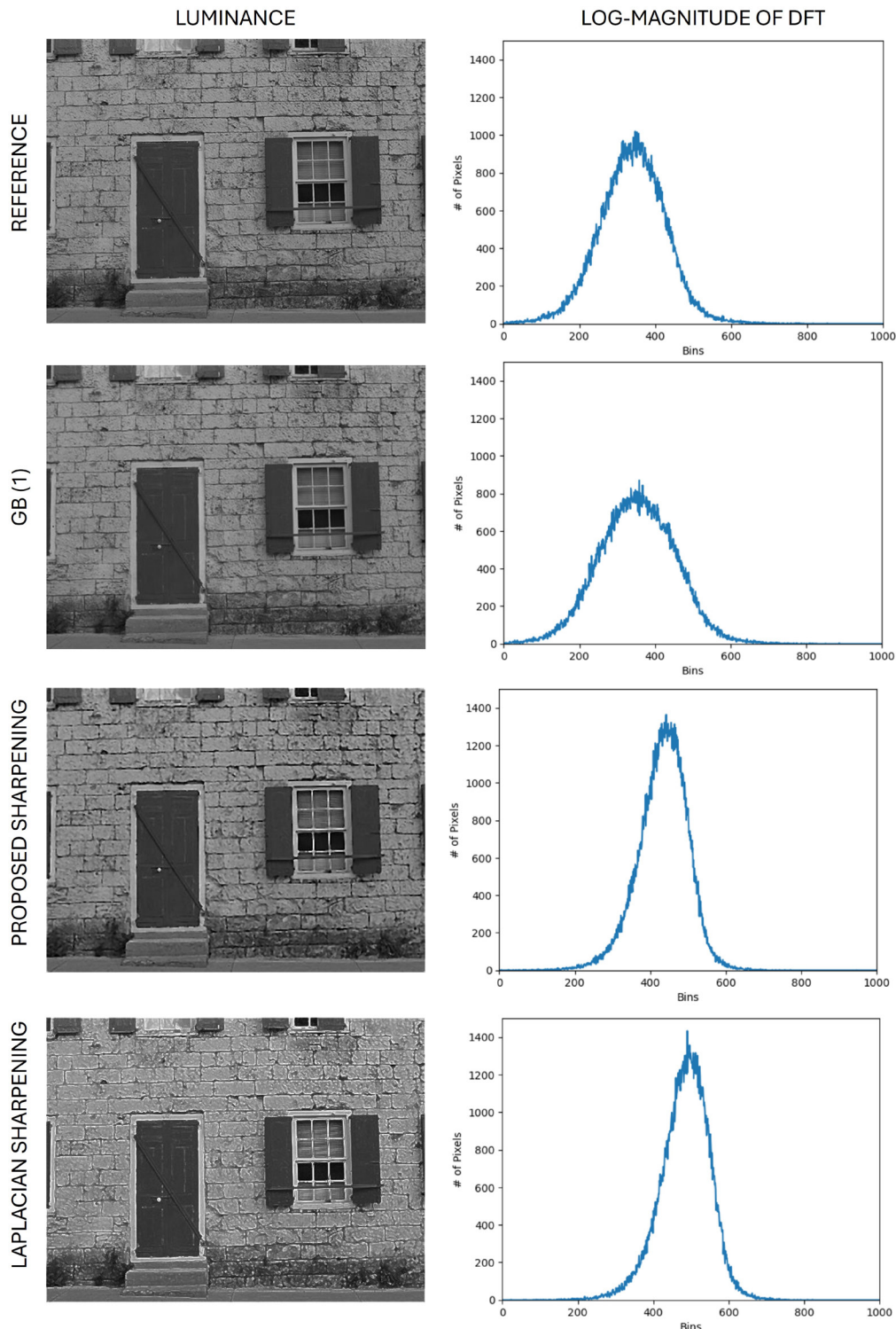


**FIGURE 28.** This pictures shows: on left, the luminances of a reference image, its version blurred by GB(1), its enhancement by the proposed sharpening filter and that by the Laplacian sharpening; on right, the histograms of the log-magnitudes of the discrete Fourier transforms of the luminances on left. The peak of the histograms of the log-magnitude of the sharpened luminances is narrower and positioned further to the right than that of the reference and blurred luminances. This indicates that the sharpened luminances contains higher frequencies than the original ones.



**FIGURE 29.** An example of JPEG compressed image from TID-2013. The reference image undergoes 5 different levels of compression indicated by JPEG-C(X) with X = 1, 2, 3, 4, 5.

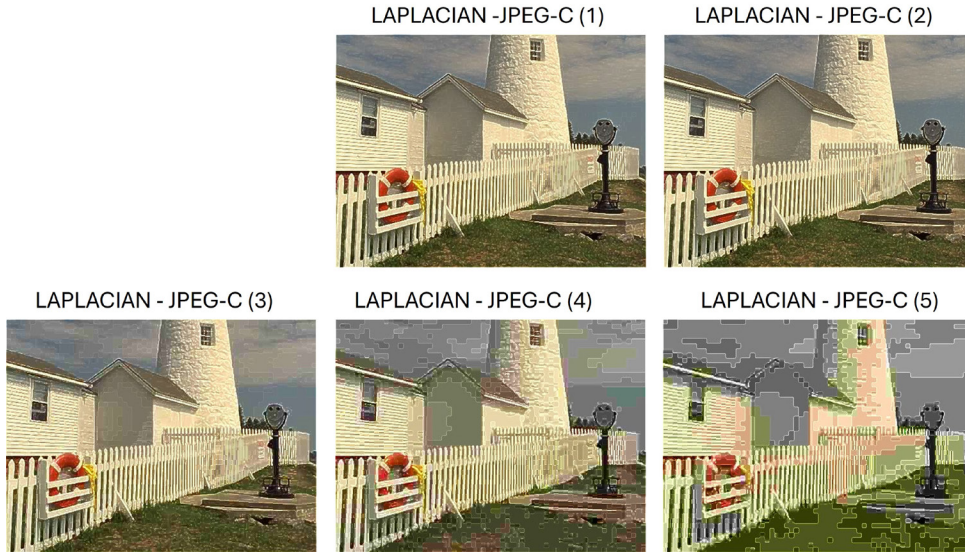


**FIGURE 30.** The JPEG compressed images in Figure 29 enhanced by the Laplacian sharpening. On all the images, the Laplacian sharpening over-enhances the edges and for the two highest compression levels the image appears like cartoonized.

whose implementation is very expensive in terms of silicon area and thus not convenient. Therefore, in the proposed image sensor architecture, the  $L * K_x$ ,  $L * K_y$  and  $M$  are directly computed on-chip and delivered to the output together with the raw image  $L$ , while the rest of the algorithm has to be implemented by an external processor.

In this framework, the column-level processing is a suitable to provide a sufficient degree of programmability, while preserving an acceptable pixel pitch. Figure 21 shows a simplified block diagram of the proposed image sensor with the three processing layers computing respectively  $L * K_x$ ,  $L * K_y$  and  $M$  on an image with size  $N \times M$ . During

image readout, the Row Decoder progressively selects the  $N$  rows of the array, so that the  $M$  pixels of each selected row are converted into a digital value by the column-level Analog-to-Digital Converters (ADC). The Raw Image in Figure 21 is delivered off-chip, row by row, by the first column decoder. The  $M$  outputs of the ADCs also feed three digital filters (MovSum, MovDiff, and MaxValue) that are used to implement  $L * K_y$ ,  $L * K_x$  and  $M$  respectively in a pipeline architecture. The output data of each filter are serially shifted and filtered before being dispatched off-chip.

The first processing layer (*Gradienty*) of Fig. 18 uses  $M$  column-level *MovSum* blocks to calculate a 3 pixel moving

**TABLE 10.** Performance Evaluation on TID-2013: the objective measures described in Section III are computed on the original images (see superscript o) distorted by JPEG compression (JPEG-C) and JPEG2000 compression (JPEG-C2) at five levels (specified by the number in the brackets) and on their versions processed by the Laplacian sharpening (see superscript l).

(a) JPEG compression												
Image Set	$L_m$	$P_m$	$\mu$	NIQE	PSNR	SSIM	$L'_m$	$P'_m$	$\mu'$	NIQE'	PSNR'	SSIM'
JPEG-C(1)	107.13	51.08	3.65	2.69	36.40	0.93	116.74	79.10	3.19	34.71	20.28	0.64
JPEG-C(2)	107.17	51.04	3.76	3.06	33.52	0.89	116.74	79.01	3.20	21.83	20.35	0.64
JPEG-C(3)	107.11	50.51	3.92	4.60	30.02	0.82	116.52	78.86	3.17	13.73	20.33	0.61
JPEG-C(4)	107.27	47.18	3.48	7.33	26.54	0.71	116.18	76.30	2.85	10.97	19.74	0.56
JPEG-C(5)	107.53	42.00	3.00	9.60	24.00	0.64	115.99	71.98	2.63	12.61	18.53	0.53

(b) JPEG2000 compression												
Image Set	$L_m$	$P_m$	$\mu$	NIQE	PSNR	SSIM	$L'_m$	$P'_m$	$\mu'$	NIQE'	PSNR'	SSIM'
JPEG-C2(1)	107.41	48.72	6.52	5.76	33.90	0.90	115.93	74.36	3.35	24.41	20.90	0.67
JPEG-C2(2)	107.39	46.85	7.27	6.19	30.82	0.84	115.26	70.56	3.54	23.16	21.17	0.66
JPEG-C2(3)	107.39	43.06	7.43	5.94	27.76	0.77	114.15	63.53	3.96	21.44	21.43	0.64
JPEG-C2(4)	107.46	36.06	6.32	6.18	24.65	0.69	112.45	51.55	4.61	15.78	21.15	0.61
JPEG-C2(5)	107.70	24.82	7.01	6.20	21.65	0.62	110.49	33.61	5.54	9.00	20.18	0.57

sum ( $P_{i-1,j} + P_{i,j} + P_{i+1,j}$ ) with  $j = 1$  to  $M$ . The  $M$  resulting values  $S_{i,j}$  are then subtracted with a block MovDiff ( $-S_{i,j} + S_{i,j+2}$ ) at the output of its column decoder, before to be delivered off-chip. The final output will be the gradient image  $L * K_y$ .

A complementary image filter (named Gradient x in Figure 21) runs in parallel with the filter Gradient y, fed with the same pixel values ( $P_{i,j}$ ), to calculate  $L * K_x$  and  $L * K_y$ . In this case, the blocks MovDiff first calculate the difference of the odd or even pixels of the same column ( $-P_{i-1} + P_{i+1,j}$ ). The  $M$  resulting values are progressively summed by a 3 pixel block MovSum before being delivered. Table 8 shows the operations that MovSum performs to compute the gradient component  $L * K_y$  as the sensor rows are read.

The second layer calculates  $L * K_x$  as the first layer, apart from the fact that the blocks MovSum and MovDiff are inverted.

The schematic of a possible implementation of the MovSum block is shown in Figure 22, together with a flow-chart describing its operations. The last filter (MaxValue) finds the maximum value of  $L$  in each sub-windows with  $5 \times 5$  pixel kernel (max L(x)). At first, the maximum value is found among the 5 pixels of the same column ( $P_{i-3,j}, \dots, P_{i+1,j}$ ). The output of this operation consists of  $M$  maximum values associated to the last 5 converted rows of the array. The  $M$  values feed a second MaxValue block, which progressively delivers the max values to the output. The three filtered output images are delivered by the sensor together with the raw image  $L$ .

The third layer calculates the maximum value of  $L$  in a sub-window. Figure 21 illustrates the case of  $5 \times 5$  pixels window (i.e.  $w = 5$ ), where the pixels of each column feed a block MaxValue that delivers the maximum value of the last 5 pixels in the column. The circuit that finds the maximum value between two n-bit data (A, B) is shown in Figure 26. It consists of  $2 \times (n+1)$  cascaded blocks. The blocks of each stage share a precharged line. During the computation of the maximum value, A and B are compared starting from

the leftmost block (MSB). For example, if  $A > B$ , with  $A_n > B_n$ , the line is pulled high by  $A_n$ , which transfers the control ( $CA_n$ ) to the (n-1)-th stage, while the control on B ( $CB_n$ ) is inhibited. At the end of this operation, the output of the network returns the value of A. The precharge signals ( $PRE_n$  to  $PRE_0$ ) are turned off with a proper delay, taking into account the propagation delay of each stage. For each new row, the maximum values are generated by comparing the past 5 rows. In conclusion, the proposed sensor architecture delivers in parallel the raw image  $L$ , the horizontal and vertical components  $L * K_x$  and  $L * K_y$  of the Prewitt's gradient and the term  $\max L$  (from the values  $M_{xy}$ ).

#### A. COMPARISON WITH SIMILAR SENSORS

Comparing the energy efficiency of a custom image sensor with other state-of-the-art sensors is usually very difficult, because hardware and software of any customized device are designed to optimize specific tasks in specifically constrained domains. Nevertheless, this Subsection presents a comparison of the proposed architecture with that of the VGA ( $640 \times 480$  pixels) image sensors described in [44]. This image sensor integrates a dynamic background subtraction algorithm on a QQVGA sub-sampled image ( $160 \times 120$  pixels) and is manufactured with a 110 nm CMOS process and powered with 3.3 V/ 1.2 V for the analog and digital parts respectively. The imager embeds two 10 bit memory/pixel resulting in a total memory of 375 kb. Despite performing different tasks, the architecture of this sensor is very similar to that one of the presented manuscript. In fact, beside the pixel array, it embeds a digital image filter directly fed by the column-level ADCs.

In the proposed sensor, assuming  $M = 160$ ,  $N=120$ , each MovSum block requires  $6 \times 8$  b memory, while MovDiff uses  $4 \times 8$  b memory. In addition to this, one M-stage column decoder is necessary to dispatch data off-chip. Thus, an additional  $160 \times 8$  b = 1.25 kb memory must be added to each Gradient layer. Therefore, to implement the layers computing the horizontal and vertical derivatives, a memory



**FIGURE 31.** The results of the proposed sharpening algorithm on the first three JPEG compressed images in Figure 29. No edge over-enhancement is visible.

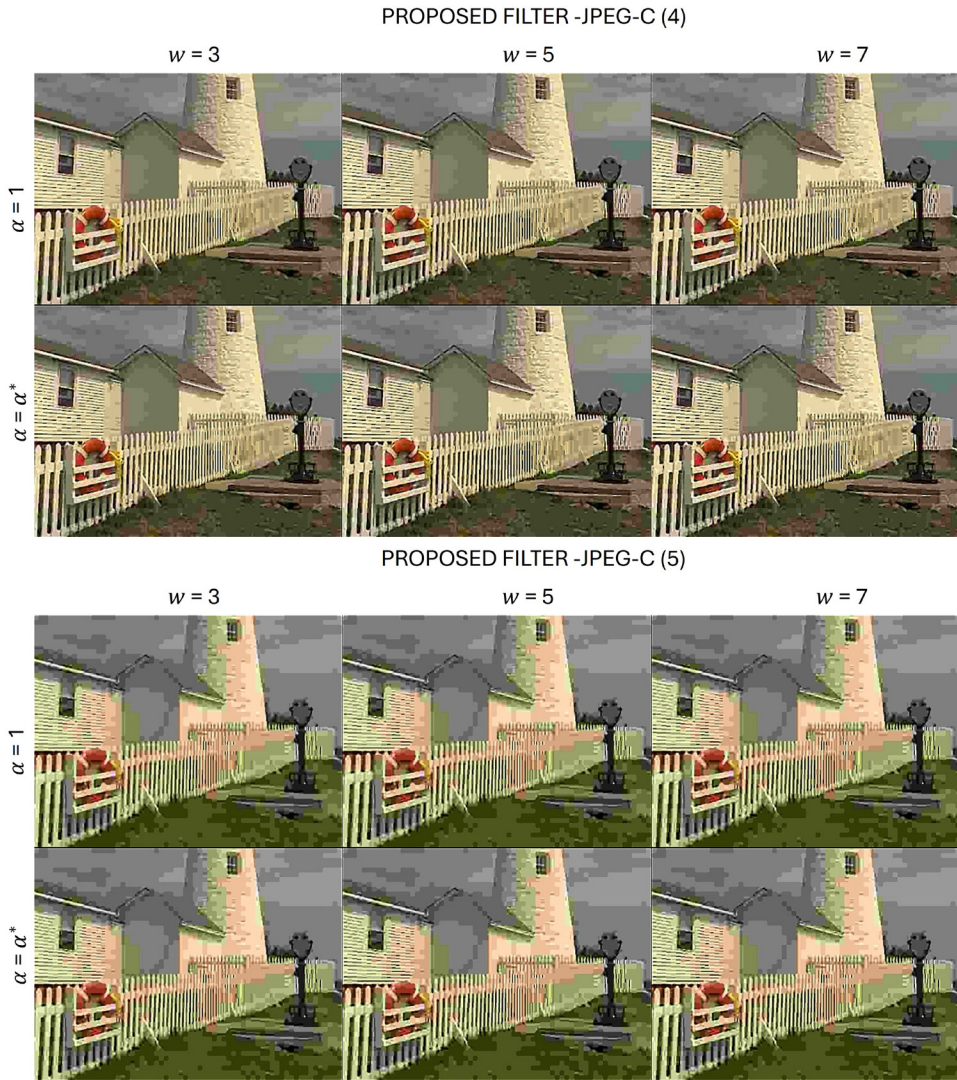


**FIGURE 32.** The results of the proposed sharpening algorithm on the last three JPEG compressed images in Figure 29. The compression of these levels is very heavy and sharpening scarcely improves the image quality.

of about 15 kb is needed. To implement the MaxValue block, each pixel to be compared needs one 8 b digital buffer. Moreover, by approximating one single stage of the MaxValue block to 1 b memory, for a total 8 b/pixel, each block Max L, working on a  $5 \times 5$  pixel kernel, will require about  $5 \times (8 \text{ b} + 8 \text{ b}) = 80 \text{ b}$ . This turns into a  $160 \times 80 \text{ b} + 1.25 \text{ kb} = 13.75 \text{ kb}$ . For a  $7 \times 7$  kernel, the memory scales up linearly to 18,75 kb.

Summarizing, the proposed sensor architecture running on a QQVGA image format and using a  $5 \times 5$  pixel kernel for the MaxValue, will require about 30 kb memory.

In Table 9, the main electrical performance of the proposed sensor are listed and compared with those of the sensor in [44], assuming that the two sensors have same number of pixels, frame rate, supply voltages and are manufactured with the same CMOS technology node. As a rough estimation, similar values for average power

consumption can be assumed for the two sensors, making the proposed architecture suitable for low power applications.

An estimation of the area of silicon occupied is made as follows. First consider a VGA sensor with a RGBW color filter array. The proposed architecture is applied only to the white pixels (W) of the array, therefore on a QQVGA image ( $320 \times 240$  pixels). Each of the 320 processing blocks (MovSum, MovDiff and MaxValue) must be organized at the column level, as shown in Figure 21. It is assumed that the three processing levels are implemented using standard 110 nm CMOS cells, where 1 bit of memory is realised with a  $33 \mu\text{m}^2$  D-type flip-flop. Since the total memory required is 30 kb (Table 9), the total amount of memory will occupy a silicon area of approximately  $1 \text{ mm}^2$ . In addition, an extra silicon area occupied by the interconnections, estimated around a further 50%, has to be added. Consequently, the total area would be  $1.5 \text{ mm}^2$ . Each single processing block

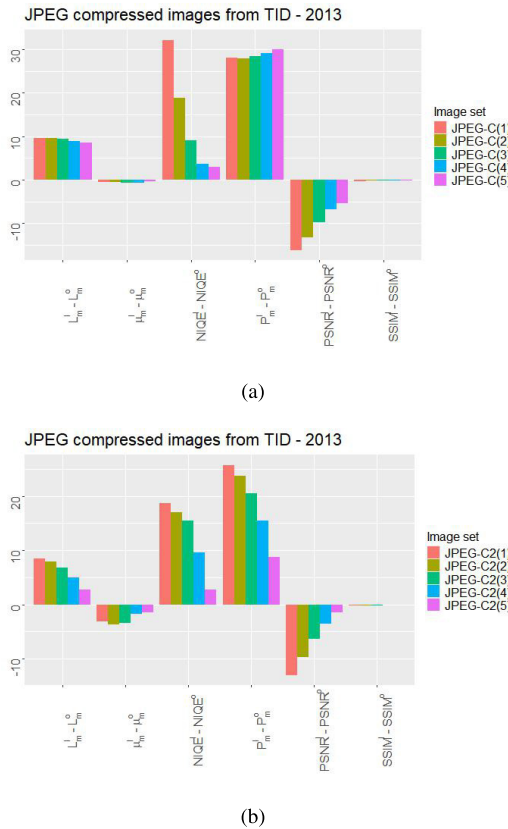


**FIGURE 33.** Subfigure (a): graphical representation of the data in Table 10 (a) and subfigure (b): graphical representation of the Table 10 (b). The length of the barplot bars is equal to the difference between the performance objective measures evaluated on the images sharpened by the Laplacian filter (superscript  $s$ ) and those evaluated on the reference images (superscript  $o$ ).

would occupy  $1.5 \text{ mm}^2 / 320 = 4700 \mu\text{m}^2$ . Assuming that the pixel pitch of the VGA sensor is  $3 \mu\text{m}$ , the pitch of each processing block at the column level must be  $6 \mu\text{m}$ , resulting in a block length of  $(4700 \mu\text{m}^2) / (6 \mu\text{m}) = 800 \mu\text{m}$ . According to this estimate, the proposed architecture can be considered compact enough to be integrated on the chip with the sensor. Further improvements can be made through full-custom design techniques.

## VI. CONCLUSION

This work proposes a new image-aware, computationally efficient spatial filter for image sharpening. This filter is defined by a  $3 \times 3$  kernel whose values are estimated without supervision from the Prewitt gradient and a Retinex inspired measure of contrast. The use of these features for sharpening has been never proposed before and represents the novelty of the approach conceived and implemented in this study. The spatial locality of the sharpening filter is controlled by a parameter  $w$ , whose typical values for images with size from  $100 \times 100$  to  $640 \times 480$  pixels are 3, 5 and 7. By default, the blending parameter  $\alpha$  in Equation (1) is set to one, but another choice of  $\alpha$ , depending on image gradient information, is also investigated in the paper (see Equation 7).

**TABLE 11.** Performance evaluation of the proposed image-aware filter on the JPEG compressed images from TID-2013 for the parameter values  $\alpha = 1$ ,  $\alpha = \alpha^*$  and  $w = 3, 5, 7$ . The compression level (JPEG-C) is indicated in the brackets.

(a) $\alpha = 1, w = 3$						
Image Set	$L_m$	$P_m$	$\mu$	NIQE	PSNR	SSIM
JPEG-C(1)	106.13	66.71	3.66	5.42	24.82	0.79
JPEG-C(2)	106.21	66.45	3.67	5.34	24.93	0.78
JPEG-C(3)	106.22	64.93	3.66	5.52	24.88	0.75
JPEG-C(4)	106.68	57.59	3.41	6.44	24.27	0.68
JPEG-C(5)	107.41	47.75	3.01	8.01	23.07	0.62
(b) $\alpha = 1, w = 5$						
Image Set	$L_m$	$P_m$	$\mu$	NIQE	PSNR	SSIM
JPEG-C(1)	106.12	75.39	3.56	5.65	23.39	0.76
JPEG-C(2)	106.18	74.68	3.57	5.59	23.54	0.75
JPEG-C(3)	106.22	72.17	3.57	5.69	23.70	0.73
JPEG-C(4)	106.66	62.17	3.35	6.53	23.62	0.67
JPEG-C(5)	107.32	49.92	2.99	7.98	22.82	0.62
(c) $\alpha = 1, w = 7$						
Image Set	$L_m$	$P_m$	$\mu$	NIQE	PSNR	SSIM
JPEG-C(1)	106.13	81.37	3.50	5.71	22.45	0.74
JPEG-C(2)	106.19	80.54	3.51	5.69	22.61	0.73
JPEG-C(3)	106.20	76.84	3.52	5.78	22.94	0.71
JPEG-C(4)	106.62	64.94	3.31	6.59	23.20	0.66
JPEG-C(5)	107.30	51.12	2.98	7.99	22.67	0.62
(d) $\alpha = \alpha^*, w = 3$						
Image Set	$L_m$	$P_m$	$\mu$	NIQE	PSNR	SSIM
JPEG-C(1)	106.08	69.81	3.60	5.50	23.83	0.78
JPEG-C(2)	106.22	71.58	3.59	5.42	23.58	0.76
JPEG-C(3)	106.25	71.90	3.59	5.68	23.30	0.72
JPEG-C(4)	106.72	65.70	3.32	6.65	22.64	0.66
JPEG-C(5)	107.42	53.74	2.96	8.03	21.97	0.61
(e) $\alpha = \alpha^*, w = 5$						
Image Set	$L_m$	$P_m$	$\mu$	NIQE	PSNR	SSIM
JPEG-C(1)	105.98	71.90	3.58	5.55	23.57	0.77
JPEG-C(2)	106.11	74.21	3.56	5.51	23.19	0.75
JPEG-C(3)	106.18	74.65	3.55	5.75	22.89	0.71
JPEG-C(4)	106.70	68.82	3.29	6.69	22.21	0.65
JPEG-C(5)	107.42	56.24	2.94	8.07	21.66	0.60
(f) $\alpha = \alpha^*, w = 7$						
Image Set	$L_m$	$P_m$	$\mu$	NIQE	PSNR	SSIM
JPEG-C(1)	105.92	72.17	3.59	5.54	23.61	0.77
JPEG-C(2)	106.05	74.89	3.55	5.59	23.18	0.75
JPEG-C(3)	106.11	75.42	3.55	5.77	22.83	0.71
JPEG-C(4)	106.63	70.13	3.27	6.72	22.01	0.64
JPEG-C(5)	107.42	57.46	2.93	8.08	21.49	0.60

The experiments carried out on 850 real-world images, show that the proposed method provides good performance for any value of  $\alpha$  and  $w$  considered here, also in comparison with the Laplacian sharpening and other popular algorithms described in Appendix B-A.

The specific application of the filter on retinal fundus images, which are often compromised by noise and low contrast, shows that the filter is particularly effective in increasing the visibility of fine details and blood vessels in the retina and is a valuable aid for computerized diagnosis procedures of the ocular fundus. A possible integration on-chip of the filter modules computing the horizontal and vertical gradients and the local maximum luminances is described. This draft hardware architecture could be used as a starting point for embedding the proposed sharpening

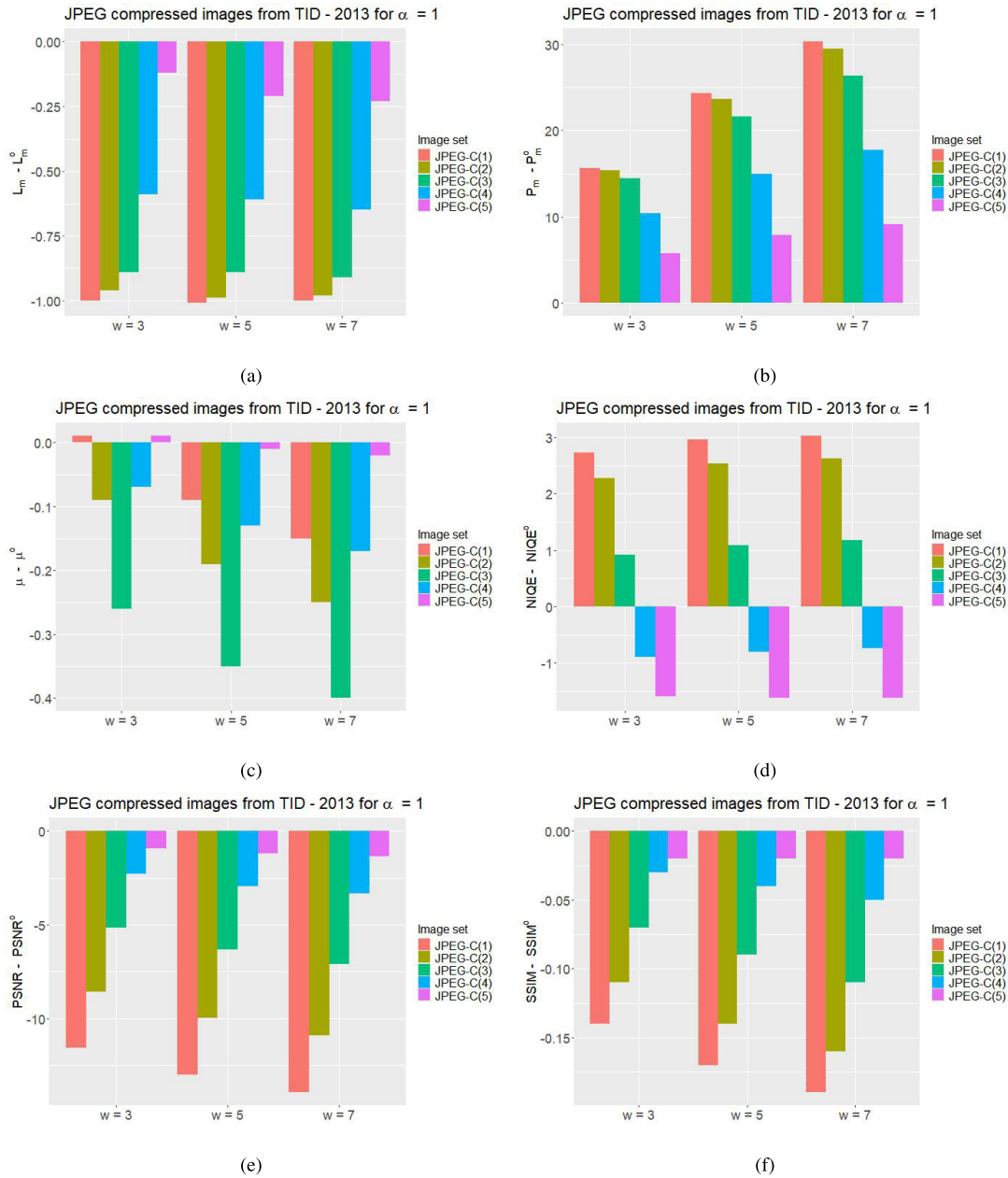


**FIGURE 34.** Graphical representation of the data in Table 11 (a), (b), and (c). The length of the barplot bars is equal to the difference between the performance objective measures evaluated on the images sharpened by the Laplacian-like sharpening filter and those evaluated on the images not subjected to sharpening (superscript o). After the sharpening procedure,  $P_m$  is increased in 100% of cases,  $\mu$  is decreased in 73.3% of cases. PSNR is decreased in all the cases, and undergoes a maximum decrease in value of approximately 13. SSIM is decreased in 100% of cases, but the decrement does not exceed 0.18.  $L_m$  is slightly decreased in all the cases, but the decrement does not exceed 1. NIQE is increased in 60% of cases, where the increment does not exceed 3. In the remaining 40% of cases, NIQE is reduced by a maximum of 1.5.

on devices with limited power resources like UAVs, whose images are often blurred because of device instabilities, weather conditions, pollution. Although the proposed sensor architecture uses very standard digital building blocks, there is enough room for design optimization aimed at matching the filter structures with an acceptable pixel pitch.

Based on the mathematical properties and experimental results reported in Appendix A and Section III, future work will address two main research lines.

The first study concerns the use of the proposed filter for detecting edges and keypoints. As explained in Sections I and II and in Appendix A, the kernel  $K_F$  is linearly related to a kernel used for approximating numerically the Laplacian operator. Due to this property, the proposed approach can be considered as a Laplacian-like sharpening algorithm, i.e. as a Laplacian sharpening but with the advantage that there are no parameters to be set by the user. As the Laplacian filter, the proposed one can be used as a zero-crossing edge

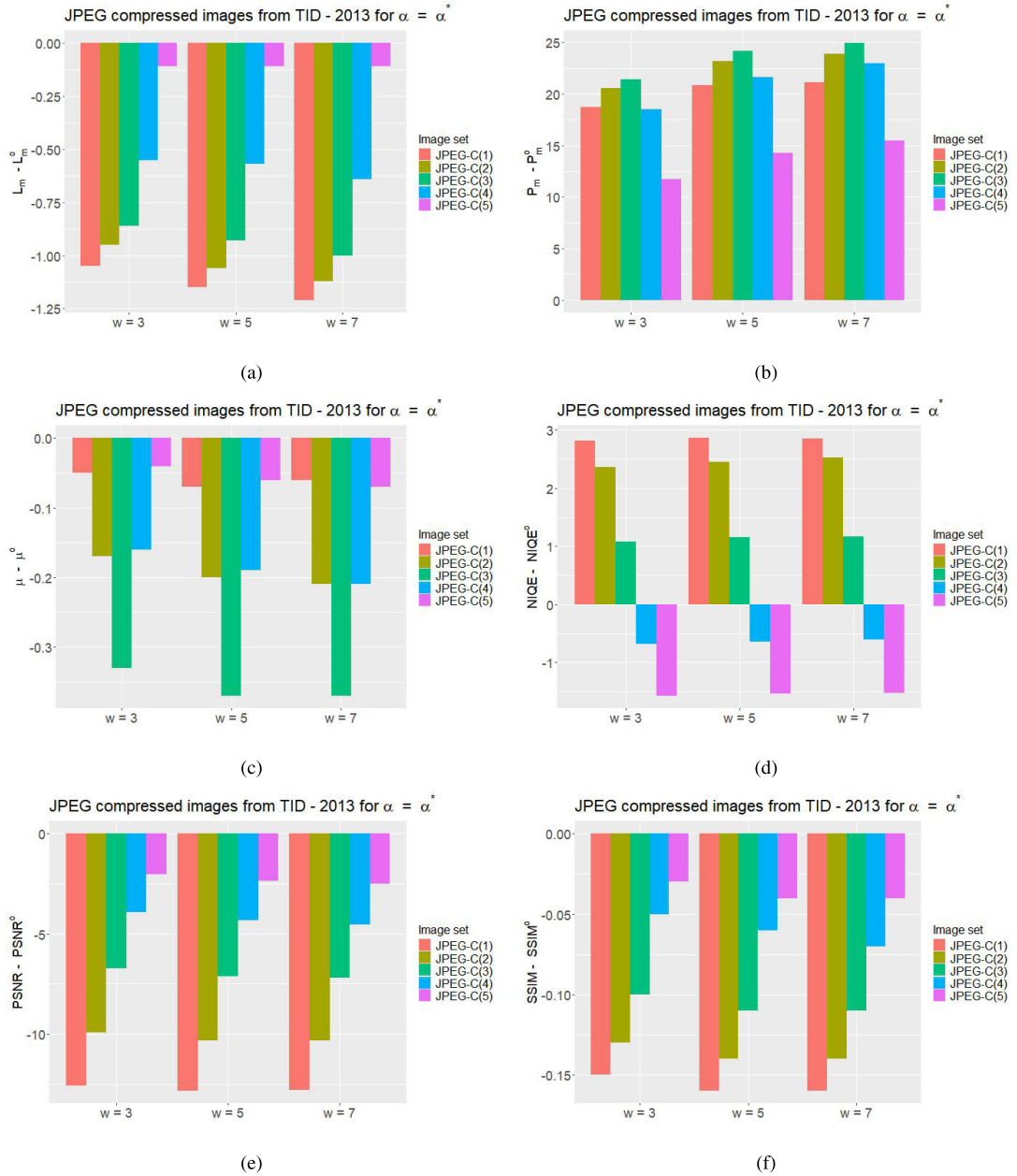


**FIGURE 35.** Graphical representation of the data in 11 (d), (e), and (f). The length of the barplot bars is equal to the difference between the performance objective measures evaluated on the images sharpened by the Laplacian-like sharpening filter and those evaluated on the images not subjected to sharpening (superscript o). After the sharpening procedure,  $P_m$  is increased in 100% of cases,  $\mu$  is decreased in all the cases. PSNR is decreased in all the cases, and undergoes a maximum decrease in value of approximately 13. SSIM is decreased in 100% of cases, but the decrement does not exceed 0.17.  $L_m$  is slightly decreased in all the cases, but the decrement does not exceed 1.25. NIQE is increased in 60% of cases, where the increment does not exceed 3. In the remaining 40% of cases, NIQE is reduced by a maximum of 1.5.

detector [47]. In this framework, the less aggressive edge enhancement obtained by the proposed filter  $F$  with respect to the Laplacian one suggests that  $F$  could provide a less noisy detection of image keypoints, i.e. pixels relevant to that identify, describe, or match objects or features in the image (see [48], [49], [50]). Future research could be thus dedicated to investigate benefits and drawbacks of the use of  $F$  within the contexts of unsupervised image description,

retrieval, classification and people/object recognition and tracking.

The second study regards the fact that the proposed filter is applied over the whole image: the sharpening is performed on each pixel with the same strength that is defined by  $c$  and  $\alpha$ . This may represent a limitation when the image contains both clean and blurry regions: setting  $c$  according to the local level of edge distortions could provide better performance



**FIGURE 36.** An example of JPEG2000 compressed image from TID-2013. The reference image undergoes to 5 different levels of compression indicated by JPEG-C2000(X) with  $X = 1, 2, 3, 4, 5$ .



**FIGURE 37.** The JPEG2000 compressed images in Figure 29 enhanced by the Laplacian sharpening. On all the images, the Laplacian sharpening over-enhances the edges and for the two highest compression levels the image appears like cartoonized.

in this case. Some works in the literature have been already proposed algorithms with *adaptive* sharpening strengths, but they require making assumptions on the blur nature and distribution (see e.g. [16]). The development of an adaptive sharpening method exclusively based on the input image is thus very challenging.

#### APPENDIX A SOME MATHEMATICAL PROPERTIES OF $K_F$

The edges of a grey level image  $L$  are often detected as the pixels where the Laplacian operator  $\Delta L$  changes sign. The approaches based on this principle are usually called

zero-crossing edge detectors [47]. In the discrete image space,  $\Delta L$  can be approximated by the following convolution

$$\Delta L = (K_\Delta * L)(x) \quad (8)$$

where  $K_\Delta$  is the following  $3 \times 3$  kernel:

$$K_\Delta = \begin{bmatrix} 1 & 1 & 1 \\ 1 & -8 & 1 \\ 1 & 1 & 1 \end{bmatrix}. \quad (9)$$

As already mentioned in Section II,  $\Delta L$  can be used for sharpening, specifically Laplacian sharpening is achieved by

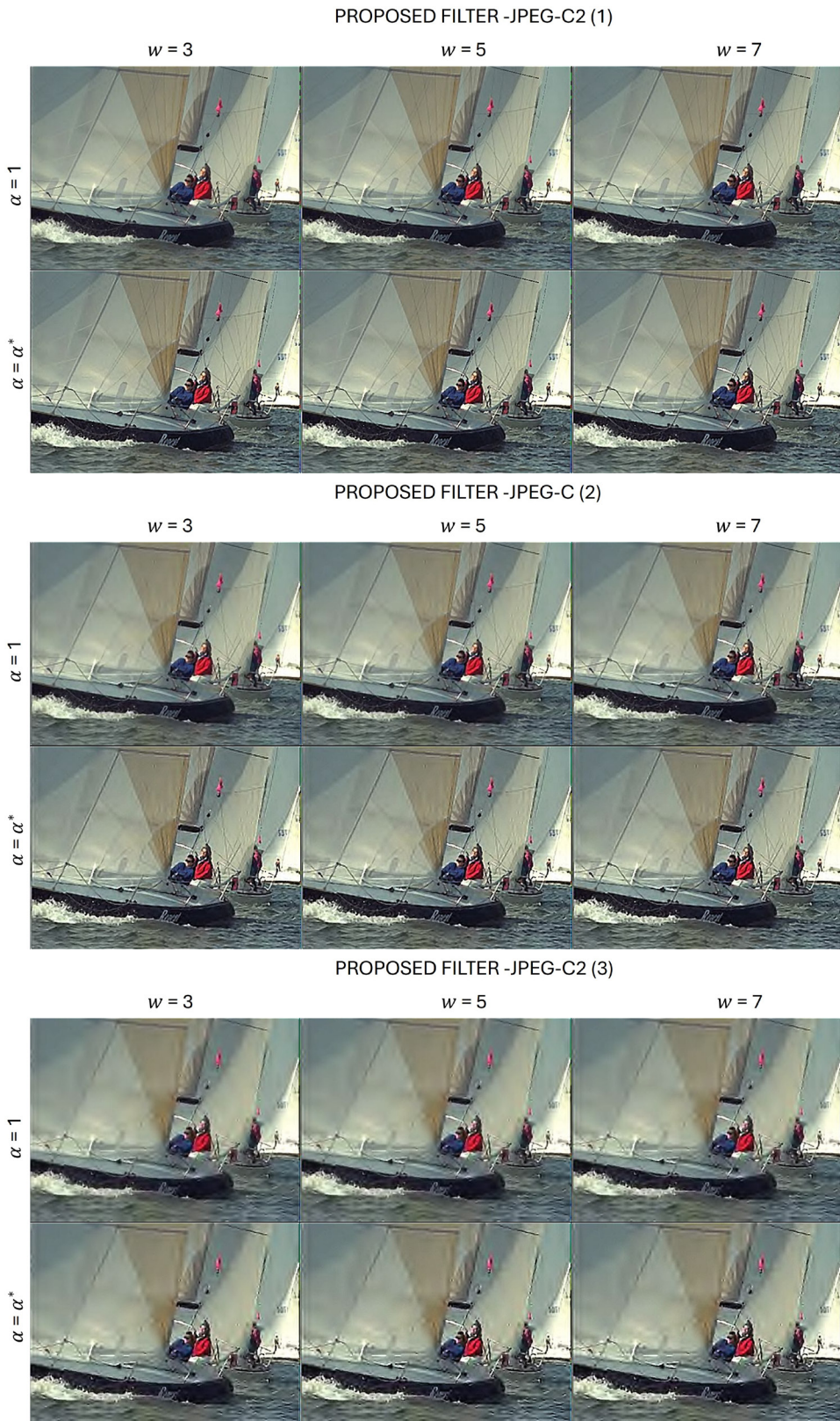


**FIGURE 38.** The results of the proposed sharpening algorithm on the first three JPEG2000 compressed images in Figure 29. No edge over-enhancement is visible.

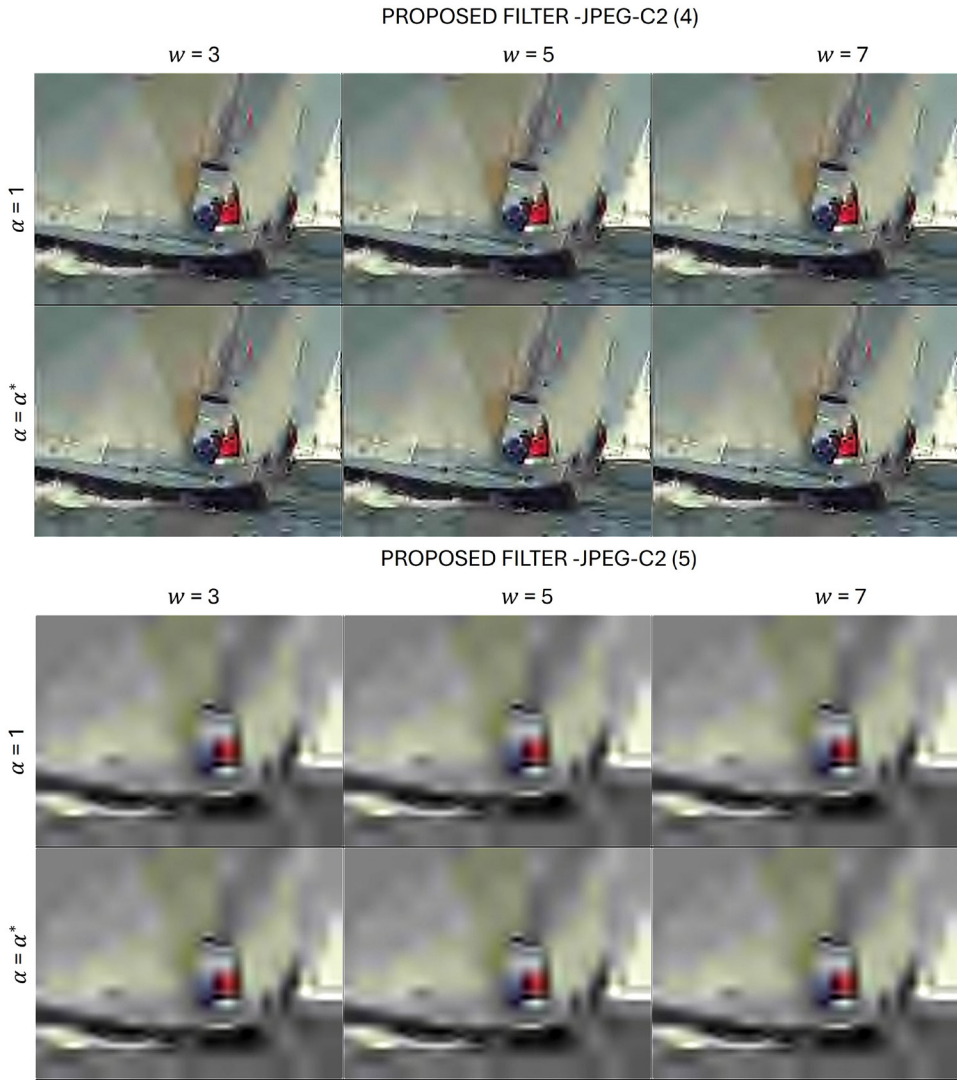


**FIGURE 39.** The results of the proposed sharpening algorithm on the last three JPEG2000 compressed images in Figure 29. The compression of these levels is very heavy and sharpening scarcely improves the image quality.

modifying Equation (1) as follows:

$$S(x) = L(x) - \alpha \Delta L \simeq L(x) - \alpha(K_\Delta * L)(x). \quad (10)$$

It can be observed that  $K_F$  is a scaled version of  $K_\Delta$ :

$$K_F = -\frac{c}{8} K_\Delta \quad (11)$$

where  $c$  is the parameter defined in Section II based on image contrast and gradient information. From Equation (11), it follows that  $K_F$  shares with  $K_\Delta$  several properties, in particular:

- 1) As  $K_\Delta$ ,  $K_F$  can be used for edge detection: in fact, the values of the images  $K_\Delta * L$  and  $K_F * L$  differ in a scale factor only, thus  $K_\Delta * L$  and  $K_F * L$  share the same zero-crossing points (see Figure 27);
- 2) When embedded within a scale-space framework,  $K_F$  is proportional to a difference of Gaussian filters with adjustable variance. In fact, the Laplacian operator

(computed with respect the spatial coordinates) of a Gaussian function  $G(x, \sigma)$  with variance  $\sigma$  satisfies the following equation:

$$\Delta G(x, \sigma) = \frac{\partial}{\partial \sigma} G(x, \sigma) \quad (12)$$

and specifically

$$\Delta G(x, \sigma) = \frac{1}{2\pi\sigma} \exp -\frac{\|x\|^2}{2\sigma} \left[ -\frac{1}{t} + \frac{\|x\|^2}{t^2} \right]. \quad (13)$$

Therefore, given two Gaussian functions with close variances  $\sigma_1$  and  $\sigma_2$ , the Laplacian operator of  $G(x, \sigma_1) * L$  can be approximated as:

$$\Delta G(x, \sigma_2) * L \simeq (G(x, \sigma_1) - G(x, \sigma_2)) * L. \quad (14)$$

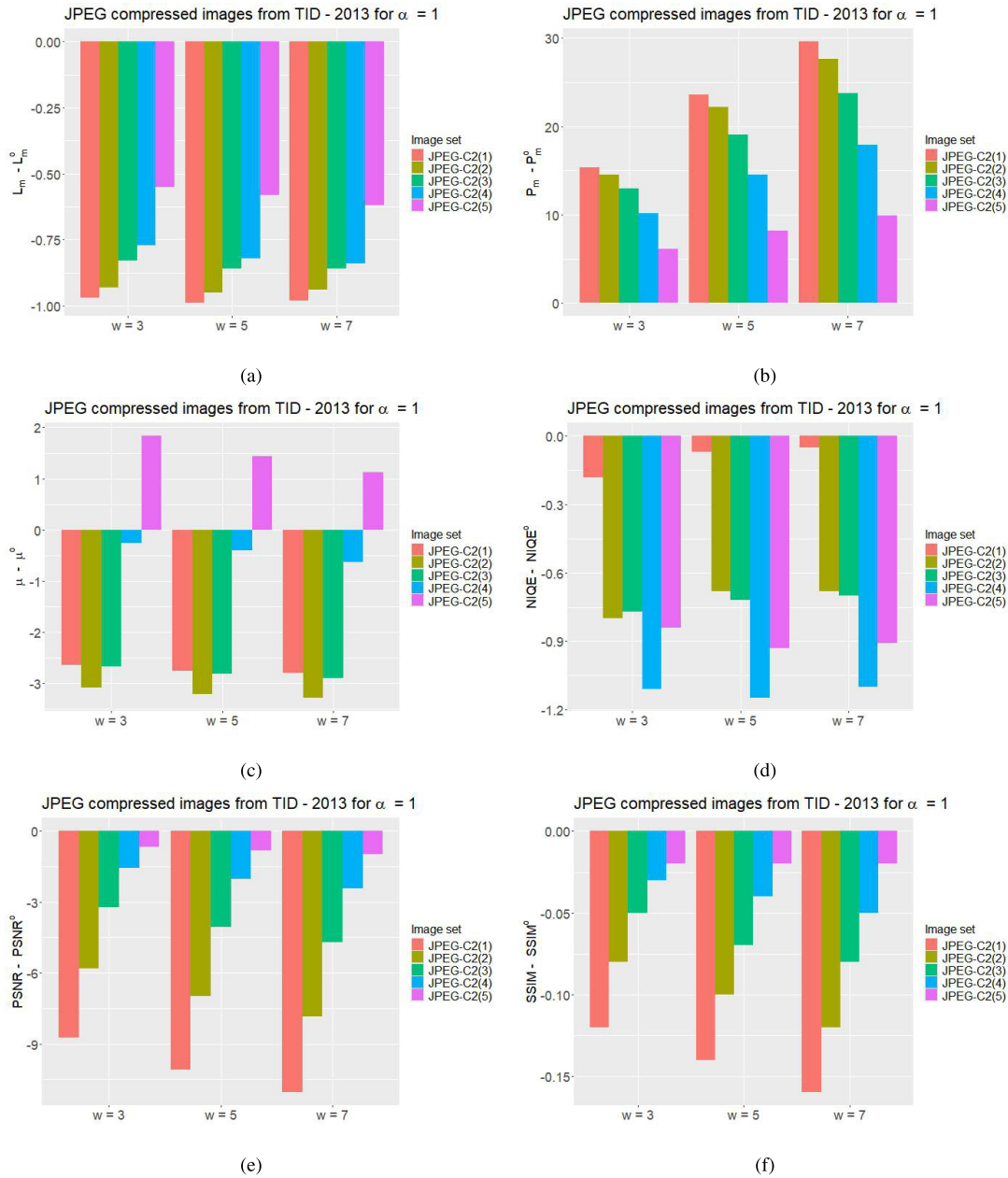


**FIGURE 40.** Graphical representation of the data in Tables 12 (a), (b), and (c). The length of the barplot bars is equal to the difference between the performance objective measures evaluated on the images sharpened by the Laplacian-like sharpening filter and those evaluated on the images not subjected to sharpening (superscript o). After the sharpening procedure,  $P_m$  is increased in 100% of cases,  $\mu$  is decreased in 80% of cases. PSNR is decreased in all the cases, and undergoes a maximum decrease in value of approximately 11.3. SSIM is decreased in 100% of cases, but the decrement does not exceed 0.17.  $L_m$  is slightly decreased in all the cases, but the decrement does not exceed 1. NIQE is decreased in all cases, and its decrement does not exceed 1.2.

It follows that

$$(K_F * G(x, \sigma_2)) * L \propto (G(x, \sigma_1) - G(x, \sigma_2)) * L. \quad (15)$$

- 3) The Fourier transforms  $\mathcal{F}$  of  $K_F * L$  and  $K_\Delta * L$  are linearly related, precisely:

$$\mathcal{F}(K_F * L) = -\frac{c}{8} \mathcal{F}(K_\Delta * L). \quad (16)$$

Therefore, the distributions of the log-magnitude of the Fourier transforms of the two sharpening approaches are shifted to each other (see figure 28).

## APPENDIX B APPLICATION TO IMAGE COMPRESSION

This Appendix reports on the use of the proposed sharpening filter in the context of image compression.

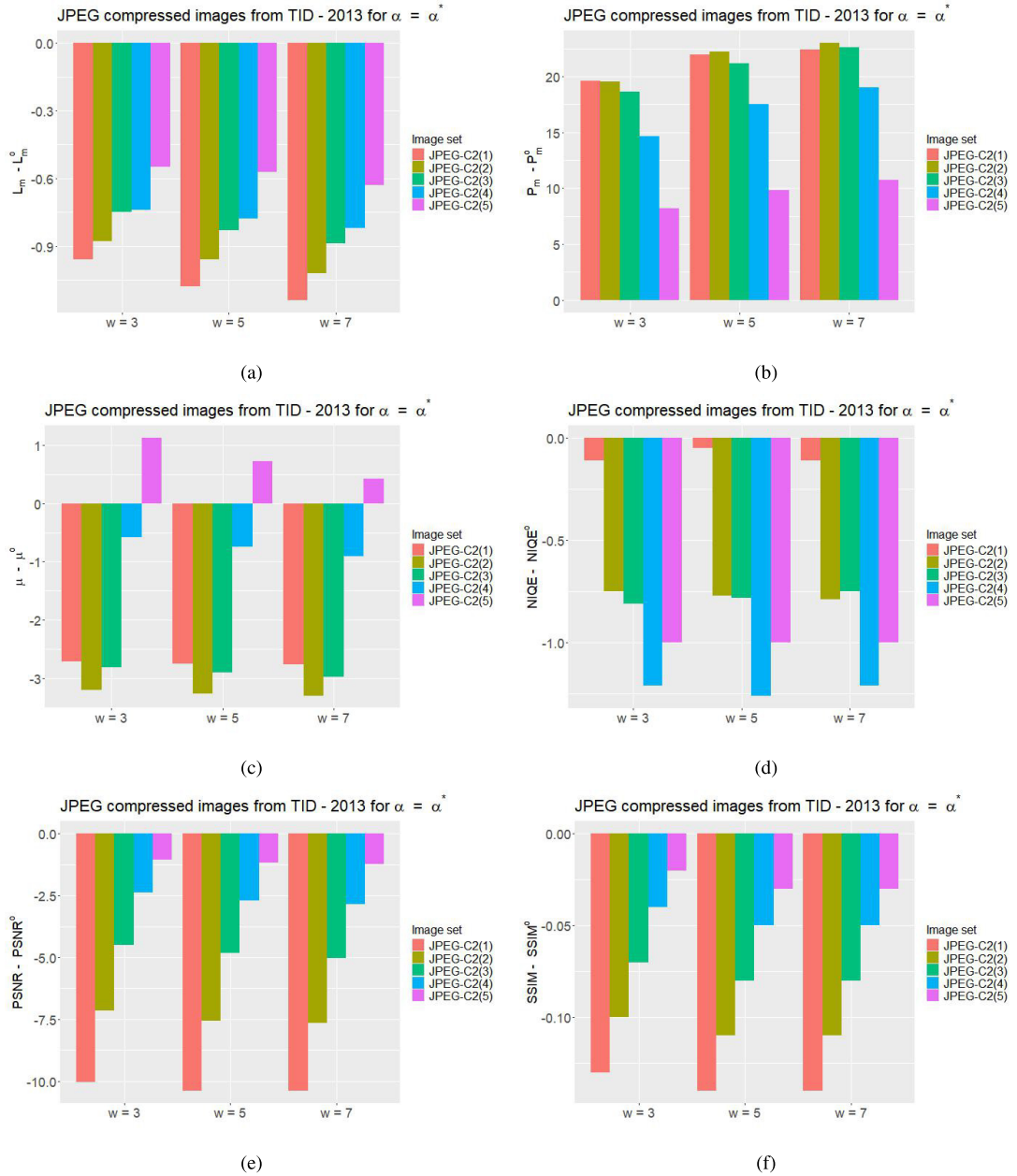


**FIGURE 41.** Graphical representation of the data in Tables 12 (d), (e), and (f). The length of the barplot bars is equal to the difference between the performance objective measures evaluated on the images sharpened by the Laplacian-like sharpening filter and those evaluated on the images not subjected to sharpening (superscript o). After the sharpening procedure,  $P_m$  is increased in 100% of cases,  $\mu$  is decreased in 80% of cases. PSNR is decreased in all the cases, and undergoes a maximum decrease slightly above 10. SSIM is decreased in 100% of cases, but the decrement does not exceed 0.92.  $L_m$  is slightly decreased in all the cases, but the decrement does not exceed 1. NIQE is decreased in all cases, and its decrement does not exceed 0.13.

In the paper, the sharpening filter has been tested on four different case studies. Specifically, it has been used and evaluated as a tool for improving the quality of images affected by synthetic Gaussian blur (TID-2013 with GB distortions), low-light (MEXICO dataset), opacity, instability and structural features of the object of interest (Kaggle Retina Blood Vessels segmentation dataset), device instability, bad weather and environmental conditions (Kaggle Remote

sensing dataset). In these contexts, the quality of the acquired image is in general uncontrollable or only poorly controllable, because it depends on external conditions. On the contrary, in the context of image compression, the quality of the image edges is voluntarily modified to enable a more efficient storage and transmission of the visual data. Precisely, the image compression algorithms rework the visual information in the spatial frequency domain and remove redundant and/or

**TABLE 12.** Performance Evaluation of the proposed image-aware filter on the JPEG2000 compressed images from TID-2013 for the parameter values  $\alpha = 1, \alpha^*$  and  $w = 3, 5, 7$ . The compression level (JPEG-C2) is indicated in the brackets.

(a) $\alpha = 1, w = 3$						
Image Set	$L_m$	$P_m$	$\mu$	NIQE	PSNR	SSIM
JPEG-C2(1)	106.44	64.04	3.88	5.58	25.17	0.78
JPEG-C2(2)	106.46	61.41	4.19	5.39	25.01	0.76
JPEG-C2(3)	106.56	55.99	4.76	5.17	24.53	0.72
JPEG-C2(4)	106.69	46.25	6.06	5.07	23.08	0.66
JPEG-C2(5)	107.15	30.97	8.84	5.36	20.98	0.60
(b) $\alpha = 1, w = 5$						
Image Set	$L_m$	$P_m$	$\mu$	NIQE	PSNR	SSIM
JPEG-C2(1)	106.42	72.30	3.77	5.69	23.80	0.76
JPEG-C2(2)	106.44	69.00	4.05	5.51	23.83	0.74
JPEG-C2(3)	106.53	62.11	4.62	5.22	23.70	0.70
JPEG-C2(4)	106.64	50.60	5.91	5.03	22.62	0.65
JPEG-C2(5)	107.12	32.97	8.45	5.27	20.84	0.60
(c) $\alpha = 1, w = 7$						
Image Set	$L_m$	$P_m$	$\mu$	NIQE	PSNR	SSIM
JPEG-C2(1)	106.43	78.28	3.72	5.71	22.84	0.74
JPEG-C2(2)	106.45	74.48	3.98	5.51	22.97	0.72
JPEG-C2(3)	106.53	66.79	4.53	5.24	23.06	0.69
JPEG-C2(4)	106.62	53.99	5.69	5.08	22.24	0.64
JPEG-C2(5)	107.08	34.76	8.13	5.29	20.69	0.60
(d) $\alpha = \alpha^*, w = 3$						
Image Set	$L_m$	$P_m$	$\mu$	NIQE	PSNR	SSIM
JPEG-C2(1)	106.45	68.31	3.81	5.65	23.87	0.77
JPEG-C2(2)	106.51	66.41	4.07	5.44	23.67	0.74
JPEG-C2(3)	106.64	61.68	4.61	5.13	23.27	0.70
JPEG-C2(4)	106.72	50.74	5.74	4.97	22.26	0.65
JPEG-C2(5)	107.15	33.03	8.13	5.20	20.61	0.60
(e) $\alpha = \alpha^*, w = 5$						
Image Set	$L_m$	$P_m$	$\mu$	NIQE	PSNR	SSIM
JPEG-C2(1)	106.33	70.69	3.77	5.71	23.51	0.76
JPEG-C2(2)	106.43	69.09	4.01	5.42	23.26	0.73
JPEG-C2(3)	106.56	64.24	4.53	5.16	22.93	0.69
JPEG-C2(4)	106.68	53.58	5.57	4.92	21.96	0.64
JPEG-C2(5)	107.13	34.64	7.73	5.20	20.49	0.59
(f) $\alpha = \alpha^*, w = 7$						
Image Set	$L_m$	$P_m$	$\mu$	NIQE	PSNR	SSIM
JPEG-C2(1)	106.27	71.14	3.76	5.65	23.51	0.76
JPEG-C2(2)	106.37	69.82	3.97	5.40	23.17	0.73
JPEG-C2(3)	106.50	65.66	4.45	5.19	22.74	0.69
JPEG-C2(4)	106.64	55.11	5.41	4.97	21.80	0.64
JPEG-C2(5)	107.07	35.56	7.43	5.20	20.42	0.59

less significant details, lowering the overall image quality. Although the detail loss due to the compression is irreversible, image sharpening can be applied to improve the quality of the edges in the compressed image.

This Appendix reports the results obtained by the standard Laplacian sharpening and the proposed one on the images from TID-2013 compressed by JPEG and JPEG2000 at five different levels. The test set considered here thus contains 250 images, each of which with size  $512 \times 384$  pixels. Basically, the JPEG and the JPEG 2000 compressions encode the visual information of the input image by the quantized coefficients of the discrete cosine transform and of the wavelets respectively. The level of the coefficients' quantization is related to the frequency details that the compression discards. Two examples of images compressed

by JPEG and JPEG2000 at different quantization levels and of their enhancement by the Laplacian sharpening and by the proposed one for different values of  $\alpha$  and  $w$  are shown in Figures 29, 30, 31, 32, 36, 37, 38 and 39. The trend of the evaluation measures for the sharpened JPEG and JPEG2000 compressed images is very similar to that of the Gaussian blurred images. In particular from Tables 10, 11, 12 (and related Figures 33, 34, 35, 40, and 41), it comes out that the Laplacian sharpening increases the brightness and the contrast of the images but also reduces their naturalness (NIQE), their similarity with the reference (SSIM) and the peak-signal-to-noise-ratio (PSNR). The sharpening obtained by the proposed filter performs better: while it increases the edge visibility a little less, it generally avoids over-sharpening, keeps the brightness more or less constant and provides better values of NIQE, SSIM, PNSR. Nevertheless, both the Laplacian sharpening and the proposed one perform poorly on the images with compression levels 4 and 5. As visible from Figures 32 and 39, for these compression levels, both the sharpening algorithms tend to emphasize the pixelized appearance of the JPEG compressed images, while their effect is negligible on the JPEG2000 compressed images whose edges still remain poorly visible. Moreover, both the sharpening algorithms (which are applied here on the luminance channel only) can neither remove nor mitigate the color artifacts present in the JPEG and JPEG2000 compression levels 4 and 5. Additionally, for these quantization levels the low frequency levels are practically lost and sharpening can only emphasize the already high frequency, returning still a low quality image.

#### A. FURTHER COMPARISONS

In Section III-D, the proposed sharpening filter has been compared with that based on Laplacian kernel. Two reasons motivated this choice. First, these two sharpening filters have similar mathematical form and computational complexity. Second, the Laplacian sharpening can be seen as a *limit case* of the proposed one, that occurs when  $c$  is set to 8 for all the image pixels. Nevertheless, for sake of completeness, this appendix shows and discusses some results achieved on the Gaussian blurred images of TID-2013 by the histogram equalization method (HE), the unsharp masking (UM) and the non-local-means based filter (NLM). Here, UM and NLM are implemented by code freely available at [51]. The experiments are here conducted on the Gaussian blurred images from TID-2013.

HE increases the visibility of image details by redistributing the image colors so that their probability density function becomes similar to an uniform one. One of the main advantages of HE is that it does require the user to set up any threshold.

Both UM and NLM adopt a slight variation of Equation (1), precisely:

$$S(x) = \beta I(x) - \alpha(I * F)(x). \quad (17)$$

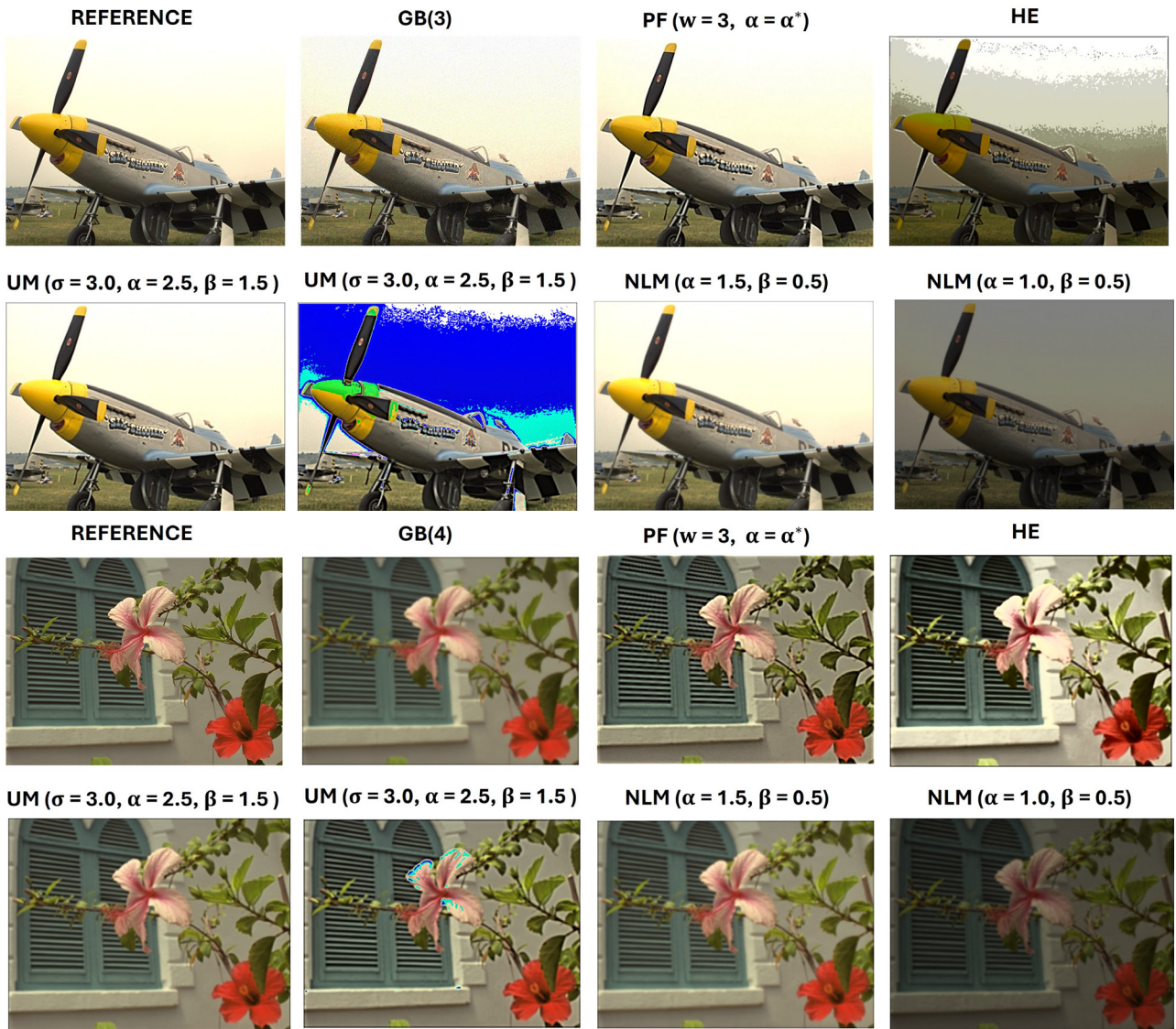


**FIGURE 42.** Comparison of the proposed filter (PF) with HE, UM and NLM on two images from TID-2013. Increasing the value of the UM parameter  $\sigma$  introduces relevant artifacts, while lowering the value of ' $\alpha$ ' makes the image sharpened by NLM quite dark.

In UM,  $\beta = 1 + \alpha$  and  $F$  is a Gaussian function whose variance  $\sigma$  is usually computed on a  $3 \times 3$  window. In NLM,  $\beta$  and  $\alpha$  are independent of each other and  $F$  is a denoising operator processing the image luminance on patches of different sizes. Both UM and NLM require the user to set the parameters of  $F$  as well as the blending coefficients  $\alpha$  for UM and  $\beta$  for NLM. In [51], by default,  $\sigma = 1.5$ ,  $\alpha = 1.5$ ,  $\beta = 0.5$ .

Some examples of sharpening by these algorithms are shown in Figure 42. Tables 13 (a), (b) and (c) report the performance of HE, UM and NLM with the parameters' values set by default. For all these algorithms, the sharpened images have a higher brightness than the corresponding references. The edges are remarkably magnified by HE, but the sharpened images are quite noisy and structurally far from their references, as indicated by the low values of PSNR

and SSIM. NLM returns the lowest values of  $P_m$ , which remain close to those of the original images, meaning that the edge visibility is only slightly improved. However, due to the denoising operator, NLM returns the highest values of PSNR and SSIM. UM generally performs well, but, apart from the case of GB(1), where the sharpened images have the highest values of  $P_m$ , its results are comparable with those provided by the proposed filter, especially for  $\alpha = \alpha^*$ . It is worth to note that setting properly the filter parameters is crucial for the final results. In fact, as illustrated by the examples in Figure 42, for  $\sigma = 3$  (and  $\alpha = 1.5$ ), UM generates noticeable color distortions, while the values of  $\alpha$  and  $\beta$  strongly affect the overall image brightness, as shown by the results of NLM for the pairs  $(\alpha = 1.5, \beta = 0.5)$  and  $(\alpha = 1.0, \beta = 0.5)$ . In this framework, the unsupervised, image-aware estimate of the parameters  $c$  and  $\alpha$  discussed

**TABLE 13.** Performance evaluation on TID-2013: the objective measures described in Section III are evaluated on the images of TID-2013 with Gaussian blur sharpened by HE, UM and NLM (as specified by the superscripts) For UM and NL the parameters have the default values specified in [51].

(a) HE						
Image Set	$L_m^{\text{HE}}$	$P_m^{\text{HE}}$	$\mu^{\text{HE}}$	$\text{NIQE}^{\text{HE}}$	$\text{PSNR}^{\text{HE}}$	$\text{SSIM}^{\text{HE}}$
GB(1)	115.94	109.42	3.18	4.44	16.40	0.68
GB(2)	116.80	98.69	3.41	4.16	16.48	0.72
GB(3)	117.58	77.50	3.86	4.66	16.02	0.70
GB(4)	117.92	50.14	4.93	5.10	15.38	0.61
GB(5)	118.10	33.61	6.20	5.52	14.61	0.50

(b) UM						
Image Set	$L_m^{\text{UM}}$	$P_m^{\text{UM}}$	$\mu^{\text{UM}}$	$\text{NIQE}^{\text{UM}}$	$\text{PSNR}^{\text{UM}}$	$\text{SSIM}^{\text{UM}}$
GB (1)	109.60	81.08	3.23	4.05	25.64	0.89
GB (2)	109.50	70.42	3.49	4.41	26.79	0.92
GB (3)	109.41	51.91	3.97	5.22	26.08	0.85
GB (4)	109.21	31.21	5.22	5.39	23.88	0.68
GB (5)	108.77	19.90	6.64	5.52	21.81	0.59

(c) NLM						
Image Set	$L_m^{\text{NLM}}$	$P_m^{\text{NLM}}$	$\mu^{\text{NLM}}$	$\text{NIQE}^{\text{NLM}}$	$\text{PSNR}^{\text{NLM}}$	$\text{SSIM}^{\text{NLM}}$
GB(1)	109.88	50.03	3.68	3.17	31.05	0.97
GB(2)	109.78	44.82	4.05	3.73	28.90	0.92
GB(3)	109.62	36.20	4.75	4.59	26.21	0.82
GB(4)	109.35	25.73	6.14	4.99	21.63	0.69
GB (5)	108.88	18.19	7.51	5.14	22.54	0.60

in Section II represents a main advantage of the proposed filter.

## REFERENCES

- [1] R. Canady, X. Zhou, Y. Barve, D. Balasubramanian, and A. Gokhale, “Adversarially robust edge-based object detection for assuredly autonomous systems,” in *Proc. IEEE Int. Conf. Assured Autonomy (ICAA)*, Mar. 2022, pp. 97–106.
- [2] L. Jing and B. Wang, “EMNet: Edge-guided multi-level network for salient object detection in low-light images,” *Image Vis. Comput.*, vol. 143, Mar. 2024, Art. no. 104933. [Online]. Available: <https://www.sciencedirect.com/science/article/pii/S0262885624000362>
- [3] A. S. Dharma, N. Tambunan, and L. E. Sinaga, “Face recognition with edge detection and LBP feature extraction,” in *Proc. IEEE Int. Conf. Comput. Sci. Inf. Technol. (ICOSNIKOM)*, Oct. 2022, pp. 1–7.
- [4] F. Orujov, R. Maskeliūnas, R. Damaševičius, and W. Wei, “Fuzzy based image edge detection algorithm for blood vessel detection in retinal images,” *Appl. Soft Comput.*, vol. 94, Sep. 2020, Art. no. 106452.
- [5] M. Vardhana, N. Arunkumar, S. Lasrado, E. Abdulhay, and G. Ramirez-Gonzalez, “Convolutional neural network for bio-medical image segmentation with hardware acceleration,” *Cognit. Syst. Res.*, vol. 50, pp. 10–14, Aug. 2018. [Online]. Available: <https://www.sciencedirect.com/science/article/pii/S1389041718300469>
- [6] M. Lecca, A. Rizzi, and R. P. Serapioni, “GRASS: A gradient-based random sampling scheme for Milan retinex,” *IEEE Trans. Image Process.*, vol. 26, no. 6, pp. 2767–2780, Jun. 2017.
- [7] K. Kaur, N. Jindal, and K. Singh, “Fractional Fourier transform based Riesz fractional derivative approach for edge detection and its application in image enhancement,” *Signal Process.*, vol. 180, Mar. 2021, Art. no. 107852.
- [8] Y. Wu, H. Guo, C. Chakraborty, M. R. Khosravi, S. Berretti, and S. Wan, “Edge computing driven low-light image dynamic enhancement for object detection,” *IEEE Trans. Netw. Sci. Eng.*, vol. 10, no. 5, pp. 3086–3098, Sep. 2023.
- [9] K. G. Dhal, A. Das, S. Ray, J. Gálvez, and S. Das, “Histogram equalization variants as optimization problems: A review,” *Arch. Comput. Methods Eng.*, vol. 28, no. 3, pp. 1471–1496, May 2021.
- [10] G. Simone, M. Lecca, G. Gianini, and A. Rizzi, “Survey of methods and evaluation of retinex-inspired image enhancers,” *J. Electron. Imag.*, vol. 31, no. 6, Dec. 2022, Art. no. 063055.
- [11] C. Li, C. Guo, L. Han, J. Jiang, M.-M. Cheng, J. Gu, and C. C. Loy, “Low-light image and video enhancement using deep learning: A survey,” *IEEE Trans. Pattern Anal. Mach. Intell.*, vol. 44, no. 12, pp. 9396–9416, Dec. 2022.
- [12] S. A. Broughton and K. Bryan, *Discrete Fourier Analysis and Wavelets: Applications to Signal and Image Processing*. Hoboken, NJ, USA: Wiley, 2018.
- [13] W. A. Mustafa, H. Yazid, W. Khairunizam, M. A. Jamlos, I. Zunaidi, Z. M. Razlan, and A. B. Shahriman, “Image enhancement based on discrete cosine transforms (DCT) and discrete wavelet transform (DWT): A review,” *IOP Conf. Ser., Mater. Sci. Eng.*, vol. 557, no. 1, 2019, Art. no. 012027.
- [14] T. D. Pham, “Kriging-weighted Laplacian kernels for grayscale image sharpening,” *IEEE Access*, vol. 10, pp. 57094–57106, 2022.
- [15] G. Deng, “A generalized unsharp masking algorithm,” *IEEE Trans. Image Process.*, vol. 20, no. 5, pp. 1249–1261, May 2011.
- [16] W. Ye and K.-K. Ma, “Blurriness-guided unsharp masking,” *IEEE Trans. Image Process.*, vol. 27, no. 9, pp. 4465–4477, Sep. 2018.
- [17] H. Kaur, D. Koundal, and V. Kadyan, “Image fusion techniques: A survey,” *Arch. Comput. methods Eng.*, vol. 28, no. 7, pp. 4425–4447, 2021.
- [18] Adobe Photoshop. *Photo Editing*. Accessed: 2020. [Online]. Available: <https://www.adobe.com/>
- [19] GIMP. *The Free & Open Source Image Editor*. Accessed: 2020. [Online]. Available: <https://www.gimp.org/>
- [20] D. Ngo, S. Lee, and B. Kang, “Nonlinear unsharp masking algorithm,” in *Proc. Int. Conf. Electron., Inf., Commun. (ICEIC)*, Jan. 2020, pp. 1–6.
- [21] M. Lecca, A. Rizzi, and R. P. Serapioni, “An image contrast measure based on Retinex principles,” *IEEE Trans. Image Process.*, vol. 30, pp. 3543–3554, 2021.
- [22] E. Land, “The Retinex,” *Amer. Scientist*, vol. 52, no. 2, pp. 247–264, 1964.
- [23] N. Ponomarenko, L. Jin, O. Ieremeiev, V. Lukin, K. Egiazarian, J. Astola, B. Vozel, K. Chehdi, M. Carli, F. Battisti, and C.-C. Jay Kuo, “Image database TID2013: Peculiarities, results and perspectives,” *Signal Process., Image Commun.*, vol. 30, pp. 57–77, Jan. 2015.
- [24] TeV Resources. *MEXICO-2020*. Accessed: Aug. 1, 2025. [Online]. Available: <https://tev.fbk.eu/resources/imageenhancement>
- [25] S. Srivastava. *From Fiction to Function: The Real Benefits of Synthetic Data*—Sheenalsrivastava. Accessed: May 25, 2025. [Online]. Available: <https://medium.com/@sheenalsrivastava/from-fiction-to-function-the-real-benefits-of-synthetic-data-6f202ec50eda>

- [26] J. Jordon, L. Szpruch, F. Houssiau, M. Bottarelli, G. Cherubin, C. Maple, S. N. Cohen, and A. Weller, "Synthetic data—What, why and how?" 2022, *arXiv:2205.03257*.
- [27] Z. Cao, Z. Wei, and G. Zhang, "A no-reference sharpness metric based on the notion of relative blur for Gaussian blurred image," *J. Vis. Commun. Image Represent.*, vol. 25, no. 7, pp. 1763–1773, Oct. 2014. [Online]. Available: <https://www.sciencedirect.com/science/article/pii/S1047320314001096>
- [28] A. Mittal, R. Soundararajan, and A. C. Bovik, "Making a 'completely blind' image quality analyzer," *IEEE Signal Process. Lett.*, vol. 20, no. 3, pp. 209–212, Mar. 2012.
- [29] R. K. Singh and R. Gorantla, "DMENet: Diabetic macular edema diagnosis using hierarchical ensemble of CNNs," *PLoS ONE*, vol. 15, no. 2, Feb. 2020, Art. no. e0220677, doi: [10.1371/journal.pone.0220677](https://doi.org/10.1371/journal.pone.0220677).
- [30] A. Diaz-Pinto, A. Colomer, V. Naranjo, S. Morales, Y. Xu, and A. F. Frangi, "Retinal image synthesis and semi-supervised learning for glaucoma assessment," *IEEE Trans. Med. Imag.*, vol. 38, no. 9, pp. 2211–2218, Sep. 2019, doi: [10.1109/TMI.2019.2903434](https://doi.org/10.1109/TMI.2019.2903434).
- [31] M. Fleckenstein, T. D. L. Keenan, R. H. Guymer, U. Chakravarthy, S. Schmitz-Valckenberg, C. C. Klaver, W. T. Wong, and E. Y. Chew, "Age-related macular degeneration," *Nature Rev. Disease Primers*, vol. 7, no. 1, May 2021, Art. no. 31, doi: [10.1038/s41572-021-00265-2](https://doi.org/10.1038/s41572-021-00265-2).
- [32] Y. Deng, L. Qiao, M. Du, C. Qu, L. Wan, J. Li, and L. Huang, "Age-related macular degeneration: Epidemiology, genetics, pathophysiology, diagnosis, and targeted therapy," *Genes Diseases*, vol. 9, no. 1, pp. 62–79, Jan. 2022, doi: [10.1016/j.gendis.2021.02.009](https://doi.org/10.1016/j.gendis.2021.02.009).
- [33] C. Wan, X. Zhou, Q. You, J. Sun, J. Shen, S. Zhu, Q. Jiang, and W. Yang, "Retinal image enhancement using cycle-constraint adversarial network," *Frontiers Med.*, vol. 8, Jan. 2022, Art. no. 793726, doi: [10.3389/fmed.2021.793726](https://doi.org/10.3389/fmed.2021.793726).
- [34] A. W. Ibrahim. (2023). *Retina Blood Vessel*. Accessed: Apr. 12, 2025. [Online]. Available: <https://www.kaggle.com/datasets/abdallahwagih/retina-blood-vessel>
- [35] A. Galdran et al., "State-of-the-art retinal vessel segmentation with minimalistic models," *Sci. Rep.*, vol. 12, 2022, Art. no. 6174, doi: [10.1038/s41598-022-09675-y](https://doi.org/10.1038/s41598-022-09675-y).
- [36] J. Shields, H. Demirci, A. Mashayekhi, R. Eagle Jr., and C. Shields, "Melanocytoma of the optic disk: A review," *Indian J. Ophthalmol.*, vol. 67, no. 12, p. 1949, 2019, doi: [10.4103/ijo.ijo\\_2039\\_19](https://doi.org/10.4103/ijo.ijo_2039_19).
- [37] A. T. Fung, J. Galvin, and T. Tran, "Epiretinal membrane: A review," *Clin. Experim. Ophthalmol.*, vol. 49, no. 3, pp. 289–308, Mar. 2021, doi: [10.1111/ceo.13914](https://doi.org/10.1111/ceo.13914).
- [38] V. Kumar, S. Azad, and P. Agarwal, "White dot fovea," *Ophthalmol. Retina*, vol. 4, no. 2, p. 186, Feb. 2020, doi: [10.1016/j.oret.2019.10.006](https://doi.org/10.1016/j.oret.2019.10.006).
- [39] Y. Tuteja. (2024). *Remote Sensing Satellite Images*. [Online]. Available: <https://www.kaggle.com/dsv/9182857>
- [40] N. Massari, M. Gottardi, L. Gonzo, D. Stoppa, and A. Simoni, "A CMOS image sensor with programmable pixel-level analog processing," *IEEE Trans. Neural Netw.*, vol. 16, no. 6, pp. 1673–1684, Nov. 2005.
- [41] N. Cottini, M. Gottardi, N. Massari, R. Passerone, and Z. Smilansky, "A 33  $\mu$ W 64  $\times$  64 pixel vision sensor embedding robust dynamic background subtraction for event detection and scene interpretation," *IEEE J. Solid-State Circuits*, vol. 48, no. 3, pp. 850–863, Mar. 2013.
- [42] J. Vohra, A. Gupta, and M. Alioto, "6.3 imager with in-sensor event detection and morphological transformations with 2.9pJ/pixel $\times$ frame object segmentation FOM for always-on surveillance in 40nm," in *IEEE Int. Solid-State Circuits Conf. (ISSCC) Dig. Tech. Papers*, Feb. 2024, pp. 104–106.
- [43] J. Choi, S. Park, J. Cho, and E. Yoon, "A 3.4 $\mu$ W CMOS image sensor with embedded feature-extraction algorithm for motion-triggered object-of-interest imaging," in *IEEE Int. Solid-State Circuits Conf. (ISSCC) Dig. Tech. Papers*, Feb. 2013, pp. 478–479.
- [44] Y. Zou, M. Gottardi, M. Lecca, and M. Perenzoni, "A low-power VGA vision sensor with embedded event detection for outdoor edge applications," *IEEE J. Solid-State Circuits*, vol. 55, no. 11, pp. 3112–3121, Nov. 2020.
- [45] M. Gottardi, L. Parmesan, P. Tosato, E. Demenev, M. Lecca, E. Manuzzato, and L. Gasparini, "A 500  $\times$  500 pixel image sensor with multiple regions of interest for center of mass-based event detection," *IEEE Sensors J.*, vol. 24, no. 20, pp. 32043–32052, Oct. 2024.
- [46] U. A. F. S. B. Mohammed. *Remote Sensing Satellite Images*. Accessed: Aug. 1, 2025. [Online]. Available: <https://www.kaggle.com/datasets/umeradnaan/remote-sensing-satellite-images>
- [47] X. Wang, "Laplacian operator-based edge detectors," *IEEE Trans. Pattern Anal. Mach. Intell.*, vol. 29, no. 5, pp. 886–890, May 2007.
- [48] G. Lowe, "Sift—the scale invariant feature transform," *Int. J.*, vol. 2, nos. 91–110, p. 2, 2004.
- [49] E. Rublee, V. Rabaud, K. Konolige, and G. Bradski, "ORB: An efficient alternative to SIFT or SURF," in *Proc. Int. Conf. Comput. Vis.*, Nov. 2011, pp. 2564–2571.
- [50] C. Liu, J. Xu, and F. Wang, "A review of keypoints' detection and feature description in image registration," *Sci. Program.*, vol. 2021, no. 1, 2021, Art. no. 8509164.
- [51] M. Kumar. *Image Sharpening*. Accessed: May 2025. [Online]. Available: <https://github.com/mayank8823/Image-Sharpening/tree/main>



**MICHELA LECCA** received the degree in mathematics from the University of Trento, Italy. She is a Senior Researcher with the Research Unit, Technologies of Vision, Digital Industry Center, Fondazione Bruno Kessler, Trento, Italy. She has co-authored more than 65 papers published in international refereed journals and conferences. She has been involved and is involved in several national and European project on machine vision and carries out an extensive review activity for many international conferences and journals. Her research interests include fundamentals of image processing, mathematical models and algorithms for color image enhancement, machine color constancy, illuminant invariant image description, low power, and smart imaging systems. She is a member of the International Association for Pattern Recognition (IAPR) and the Associazione Italiana per la Ricerca in Computer Vision, Pattern Recognition, and Machine Learning (CVPR). She is a Topical Editor of *Journal of the Optical Society of America—A*.



**MASSIMO GOTTALE** (Member, IEEE) is a Senior Researcher with the Centre for Materials and Microsystems, Fondazione Bruno Kessler, Trento, Italy. He is the co-author of more than 100 papers in refereed journals and international conferences. His current research interests include CMOS design of energy-efficient vision sensors, hardware-oriented algorithms for sensor-embedded image processing, low-power computational imaging, memristor-based architectures for adaptive sensory systems, and the Internet of Things. He served as a reviewer for several international journals.



**PAOLA LECCA** is an Assistant Professor with the Faculty of Engineering, Free University of Bozen-Bolzano, where she is carrying on research in several bioinformatics projects, as a principal investigator. She carries out a technology transfer activity with the AI-Laboratory of the Faculty of Engineering, Free University of Bozen-Bolzano, which bridges the results of research and its practical implications. She is the author of more than 150 articles in the field of mathematics and computer science applied to systems biology. She deals specifically with the development of new computational techniques in graph theory; dynamical networks modeling and analysis; network inference; and causal artificial intelligence for the analysis, interpretation, and modeling of biological and biomedical data from both molecular biology experiments and biomedical imaging. In the latter field she has won awards in conferences and serves as a project coordinator for national and regional health companies on brain tumour images processing for diagnostic purposes. Alongside her research activity, she carries out an intense editorial activity both as a Guest Editor and an Associate Editor in international journals.